Computer Methods in Applied Mechanics and Engineering 431 (2024) 117258

Contents lists available at ScienceDirect

Comput. Methods Appl. Mech. Engrg.

journal homepage: www.elsevier.com/locate/cma

High-order 3D virtual element method for linear and nonlinear elasticity

Bing-Bing Xu [a,*], Wei-Long Fan [b], Peter Wriggers [a]

[a] Institute of Continuum Mechanics, Leibniz University Hannover, Hannover, Germany
[b] School of Mechanics and Aerospace Engineering, Dalian University of Technology, Dalian, China

ARTICLE INFO

Keywords:
Virtual element method
Hyperelasticity
Nonlinear

ABSTRACT

In this work, we develop a general high-order virtual element method for three-dimensional linear and nonlinear elastic problems. Applications of the virtual element method (VEM) in three-dimensional mechanics include linear elasticity problems, finite elastic strain problems, finite deformation plasticity problems, etc. But besides linear elastic problems, see e.g. Visinoni, 2024, the numerical schemes were all based on a first-order approximation of the displacement. We derive three-dimensional elastic problems, including linear elastic problems and for the first time hyperelastic problems. Similar to previous work, we discuss the calculation method of three-dimensional high-order projection operators of vector fields and calculate the tangent stiffness matrix of elastic problems according to the variational scheme. Since traditional VEM requires the use of stabilization terms to ensure the correctness of the rank of the stiffness matrix, we give suggestions for the selection of stabilization terms for high-order virtual element methods in both linear and nonlinear elasticity. Finally, we illustrate the accuracy, convergence, and stability of the high-order VEM for elastic problems by means of some classic elastic and hyperelastic examples. In addition, we also apply the developed methodology to some complex and difficult problems which illustrate the adaptability of the method to engineering problems.

1. Introduction

Numerical simulation of elastic structures has long been a cornerstone of engineering and scientific research, allowing the prediction of structural deformations under various loading conditions as well as stress calculations. Over the last 50 years, significant progress has been made in computational methods aimed at accurately capturing the complex behavior of elastic materials, such as finite element methods, boundary element methods, meshless methods, etc. To improve the analysis capabilities of complex geometries, numerical methods based on polygon or polyhedral elements [1–6] have gained more attention. But without exception, these methods have great difficulties when processing complex polygonal elements (such as non-convex polygons or arbitrary polygons) or three-dimensional polyhedral elements. The virtual element method (VEM) introduced in [7,8] is a generalized finite element method that can be applied to polygonal or polyhedral meshes, also including non-convex and very distorted elements [9]. The basic VEM theory and code can be found in the Refs. [10–12].

In addition to the classic Poisson's equation, the virtual element method has been widely used in various mechanics and engineering problems. In the domain of linear elastic mechanics, researchers have developed different virtual element methods formats for two-dimensional and three-dimensional elastic mechanics problems [12–17]. In addition, the application of the virtual element method to nonlinear problems has also received a lot of attention and research. Current applications include

* Corresponding author.
E-mail address: bingbing.xu@ikm.uni-hannover.de (B.-B. Xu).

https://doi.org/10.1016/j.cma.2024.117258
Received 14 June 2024; Received in revised form 20 July 2024; Accepted 22 July 2024
Available online 30 July 2024

hyperelastic materials at finite deformations [18–21], contact problems [22–25] and finite elastoplastic deformations [26–28]. Besides, the VEM has been extended to the applications of topology optimization [29,30], elastodynamics problems [31–34] and phase field fracture [35,36]. Recently, the VEM was also presented for propagating uncertainty in linear elastic stochastic problems [37]. However, upon the author's analysis, it is evident that the virtual element method has predominantly been applied to two-dimensional problems, including high-order forms [15,38,39] and 2D nonlinear problems [18,21,40–42].

Inevitably, a large number of engineering and scientific problems are often three-dimensional problems. Using the virtual element method in 3D complex engineering problems will reduce the difficulty of pre-processing. Up to now, the three-dimensional virtual element method has also been developed for linear elastic problems and nonlinear problems, but mainly for low order($k = 1$) virtual elements, see e.g [14,16,27–29]. With the use of automatic differentiation tools, the virtual element method has been applied to a wider range of three-dimensional problems. For details, see the latest books in VEM [9]. However, most current applications in three-dimensional mechanics are all based on the first-order virtual element method. The first-order virtual element method has very good computational efficiency (because only a single-point integration is required). Given the appropriate technology, for example, the Taylor–Hood type virtual element formulations for incompressible strains [43], the first-order virtual element method can also achieve acceptable results. Besides, a simple and effective gradient recovery scheme has been proposed to get a more accurate displacement gradient [44]. However, due to volume locking, first-order VEM requires a mixed approach to obtain accurate results, see [28]. However, the low-order mixed method cannot alleviate locking in bending situations. This can only be overcome by higher-order schemes. (the conventional finite element method also has the same problem, but the volume-locking phenomenon in higher-order FEM will be greatly improved). Therefore, in this work, we will develop a high-order virtual element method to improve accuracy. For Poisson's equation (as well as the diffusion–reaction problem), high-order three-dimensional virtual element methods have been proposed with a high-order polynomial degree (up to $k = 10$) [45–47]. But so far, there are only a few high-order three-dimensional virtual element formulations for linear elastic problems, see [48]. But to the author's knowledge, no higher-order virtual element formulation exists for finite strain problems. In this paper, we will develop a three-dimensional high-order virtual element method for three-dimensional linear and nonlinear elasticity.

The main idea of the VEM is to split the variable $\boldsymbol{u}$ into a projection $\boldsymbol{\Pi u}$ and a remainder, which results in a stiffness matrix requiring an additional stabilization term. The selection of appropriate stabilization terms and associated parameters is an important topic, especially for nonlinear problems. Several techniques for the stabilization of virtual elements have been developed, e.g. [13–15] for linear elasticity, [18] for hyperelasticity. Generally speaking, there are often one or more parameters (called stabilization parameters) in the stabilization term. It is often found that smaller stabilization parameters can lead to better results, but also cause instability (leads to non-convergence in nonlinear calculations) at the same time. Another technique named energy stabilization (nonlinear stabilization) is adopted in [19,21] for compressible and incompressible finite deformations. However, this format requires the introduction of the shape function of the triangular or tetrahedral element in the finite element, so this will bring great inconvenience to the high-order virtual element method, especially for three-dimensional elements. To avoid the impact of stabilization terms on the results of the problem (especially for nonlinear problems), the stabilization-free virtual element method (SFVEM) [49–52] has been proposed and developed for 2D and 3D linear [53,54] and nonlinear problems [55]. The core idea of this SFVEM is to use high-order polynomials to approximate gradients or strains. However, due to the need to calculate the integral of higher-order polynomials, the required amount of calculations and calculation time is relatively large and thus SFVEM scheme will not be applied here. For high-order three-dimensional VEMs, the choice of stabilization terms is discussed in [46], but only for linear Poisson's equations. In this work, we will further discuss the parameter selection of the stabilization term of the second-order VEM in linear and nonlinear elasticity.

The paper is divided into the following parts. The basic equations of elasticity are reviewed in Section 2. Then, the function spaces and projection operators for the high-order virtual element method will be given in Section 3. Besides, the specific format of the high-order virtual element method for solving linear and nonlinear elastic mechanics problems can be found in Section 4. Section 5 gives specific application examples of the high-order virtual element method in linear elasticity and hyperelasticity problems. The conclusion and discussion will be provided in Section 6.

2. Equations of elastic mechanics

In this section, we will review the continuum-based description of the solid. We assume that a boundary domain Ω in $\mathbb{R}^3$ with Lipschitz boundary Γ is occupied by a homogeneous isotropic elastic material. The motion of the body

$$\boldsymbol{\varphi} : \Omega_0 \to \Omega = \boldsymbol{\varphi}(\Omega_0) \tag{1}$$

$$\boldsymbol{X} \mapsto \boldsymbol{x} = \boldsymbol{\varphi}(\boldsymbol{X}, t), \forall \boldsymbol{X} \in \Omega_0, t \geq 0 \tag{2}$$

maps the material coordinate $\boldsymbol{X}$ (initial configuration Ω_0) to $\boldsymbol{x}$ (current configuration Ω), so that the displacement is $\boldsymbol{u} = \boldsymbol{x} - \boldsymbol{X}$. Since $\boldsymbol{\varphi}$ is smooth and invertible, we can also define the deformation gradient

$$\boldsymbol{F} = \nabla_{\boldsymbol{X}} \boldsymbol{\varphi} = \boldsymbol{I} + \nabla_{\boldsymbol{X}} \boldsymbol{u}, \tag{3}$$

where $\nabla_{\boldsymbol{X}}$ represents the displacement gradient to the initial coordinates, $\boldsymbol{I}$ is the second-order unity tensor. The determinant of the deformation gradient is given as $J = \det(\boldsymbol{F}) > 0$.

The small strain deformation tensor is defined as a linear function of the displacement gradient $\nabla \boldsymbol{u}$ by

$$\boldsymbol{\varepsilon}(\boldsymbol{u}) = \nabla_s \boldsymbol{u} = \frac{1}{2}\left(\nabla \boldsymbol{u} + \nabla \boldsymbol{u}^T\right). \tag{4}$$

In the finite strain case, the Green–Lagrange strain tensor can be introduced as

$$\boldsymbol{E} = \frac{1}{2}(\boldsymbol{C} - \boldsymbol{I}), \tag{5}$$

where $\boldsymbol{C}$ is the right Cauchy–Green deformation tensor

$$\boldsymbol{C} = \boldsymbol{F}^T \cdot \boldsymbol{F}. \tag{6}$$

In the case of static problems, the governing equation of the solid in the current configuration Ω is

$$\nabla_{\boldsymbol{x}} \cdot \boldsymbol{\sigma} + \boldsymbol{b} = \boldsymbol{0}, \tag{7}$$

where $\boldsymbol{b}$ is the body force and $\boldsymbol{\sigma}$ is the (symmetric) Cauchy stress tensor, $\nabla_{\boldsymbol{x}}\cdot$ is the current configuration divergence operator. Using the deformation map, the governing Eq. (7) can be pulled back to the initial configuration

$$\nabla_{\boldsymbol{X}} \cdot \boldsymbol{P} + \boldsymbol{b}_0 = \boldsymbol{0}, \tag{8}$$

where $\boldsymbol{P} = J\boldsymbol{\sigma}\boldsymbol{F}^{-T}$ is the first Piola–Kirchhoff stress tensor, $\boldsymbol{b}_0 = \boldsymbol{b}(\boldsymbol{\varphi}(\boldsymbol{X}))$ is the body force in the initial configuration. To construct a work conjugated formulation, the second Piola–Kirchhoff stress tensor $\boldsymbol{S}$ is

$$\boldsymbol{S} = \boldsymbol{F}^{-1} \cdot \boldsymbol{P} = J\boldsymbol{F}^{-1} \cdot \boldsymbol{\sigma} \cdot \boldsymbol{F}^{-T}. \tag{9}$$

The elastic behavior of a deformable body can be specified in terms of a strain energy density function Ψ. In the linear cases, we compute the Cauchy stress tensor as

$$\boldsymbol{\sigma} = \frac{\partial \Psi}{\partial \boldsymbol{\varepsilon}}. \tag{10}$$

where Ψ is a homogeneous isotropic linear elastic material as

$$\Psi(\boldsymbol{\varepsilon}) = \frac{\lambda}{2}\left(\mathrm{tr}\,(\boldsymbol{\varepsilon})\right)^2 + \mu \mathrm{tr}\left(\boldsymbol{\varepsilon}^2\right), \tag{11}$$

where λ and μ are the Lame constants, which can be expressed in terms of Yong's modulus E and Poisson's ratio ν as

$$\lambda = \frac{E\nu}{(1+\nu)(1-2\nu)}, \quad \nu = \frac{E}{1(1+\nu)}. \tag{12}$$

Based on Eq. (10), the Cauchy stress tensor under small strain assumption has the formulation as

$$\boldsymbol{\sigma} = \frac{\partial \Psi}{\partial \boldsymbol{\varepsilon}} = \lambda \mathrm{tr}(\boldsymbol{\varepsilon})\boldsymbol{I} + 2\mu\boldsymbol{\varepsilon}. \tag{13}$$

For a homogeneous compressible isotropic hyperelastic material, the neo-Hookean hyperelastic model can be selected with the strain energy function as

$$\Psi = \frac{\mu}{2}(\mathrm{tr}(\boldsymbol{C}) - 3) - \mu \ln J + \frac{\lambda}{2}(\ln J)^2. \tag{14}$$

Then the second Piola–Kirchhoff stress tensor can be obtained as (note $\frac{\partial J}{\partial \boldsymbol{C}} = \frac{1}{2}J\boldsymbol{C}^{-1}$)

$$\boldsymbol{S} = 2\frac{\partial \Psi}{\partial \boldsymbol{C}} = \mu(\boldsymbol{I} - \boldsymbol{C}^{-1}) + \lambda(\ln J)\boldsymbol{C}^{-1}. \tag{15}$$

Lastly, the potential energy can be written as

$$U(\boldsymbol{u}) = \int_{\Omega}\left[\Psi(\boldsymbol{u}) - \boldsymbol{b}_0 \cdot \boldsymbol{u}\right] \mathrm{d}\Omega - \int_{\Gamma_N} \bar{\boldsymbol{t}} \cdot \boldsymbol{u}\, \mathrm{d}\Gamma, \tag{16}$$

where Γ_N is the Neumann boundary and $\bar{\boldsymbol{t}}$ is the prescribed surface traction.

3. High-order virtual element method

Next, we will describe in detail the discretization procedure for the high-order virtual element method format for small and finite strain elastic problems.

3.1. Notation

A major feature of the virtual element method is that the method allows the use of arbitrary polygons or polyhedra for model discretization. A complex geometry and its polyhedral mesh discretization process $\mathcal{T}_h = \{\Omega_h\}_h$ is shown in Fig. 1. To avoid confusion, in the following part of the paper, E will denote a polyhedral element, while faces, edges and vertices will be indicated by f, e, and v respectively. Besides, for a given polyhedral element, some parameters are given as: volume $|E|$, barycenter $\boldsymbol{x}_E = (x_E, y_E, z_E)^T$, and diameter h_E.

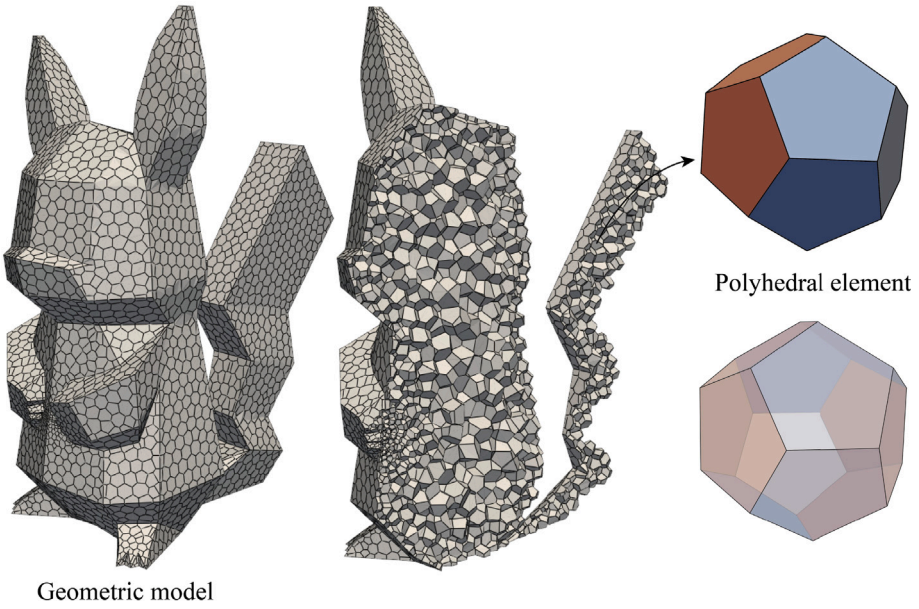

Fig. 1. Polyhedral mesh discretization of complex geometries.

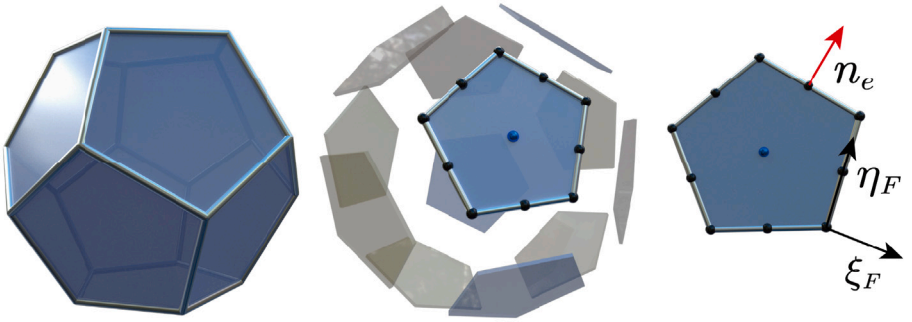

Fig. 2. Polyhedral element and its polygonal surfaces.

For a given nonnegative integer k, $\mathcal{P}_k(E)$ denotes the space of polynomials of order k and $\mathcal{M}_k(E)$ denotes the scaled monomials as

$$\mathcal{M}_k(E) := \left\{ m_\alpha = \left(\frac{\boldsymbol{x} - \boldsymbol{x}_E}{h_E} \right)^{\boldsymbol{\alpha}} \text{ for } \boldsymbol{\alpha} \in \mathbb{N}^d \text{ with } |\boldsymbol{\alpha}| \le k \right\}, \tag{17}$$

where $\boldsymbol{\alpha} = (\alpha_1, \alpha_2, \alpha_3)$ is a multiindex and $\boldsymbol{x}^{\boldsymbol{\alpha}} := x_1^{\alpha_1} \cdots x_1^{\alpha_d}$.

Different from Poisson's equation, the governing equations of elastic mechanics problems are vector field equations. We use the bold symbols, such as $\boldsymbol{u}$, $\boldsymbol{v}$, $\boldsymbol{\mathcal{H}}^1$, $\boldsymbol{\mathcal{P}}_k$, $\boldsymbol{\mathcal{V}}_k$ for the vector-valued functions or spaces.

3.2. Virtual element on polyhedron for vector-valued problems

Let Ω_h be a partition of Ω into non-overlapping polyhedrons. For each element $E \in \Omega_h$, the boundary $F \in \mathcal{F}_n$ is a polygon embedded in $\mathbb{R}^3$, which can be treated as a two-dimensional local element using local coordinates (ξ_F, η_F) as shown in Fig. 2. In the following, we use $|F|$ to represent the area of the polygon element and the subscript F to indicate the locally defined symbols.

We can follow [45] to define our function spaces. For the local vector-valued virtual element function space, we first introduce the elemental boundary space (note that $F \in \partial E$ is a 2D polygon):

$$\boldsymbol{\mathcal{B}}(\partial E) := \left\{ \boldsymbol{v} \in \boldsymbol{C}^0(\partial E) : \boldsymbol{v}|_F \in \boldsymbol{\mathcal{V}}_k^f(F), \forall F \in \partial E \right\}, \tag{18}$$

where $\boldsymbol{\mathcal{V}}_k^f(F)$ is the two-dimensional virtual element space on F. The definition of the function space for boundary elements can be found in e.g. [7,8], and is also given in Appendix A, see Eq. (A.5).

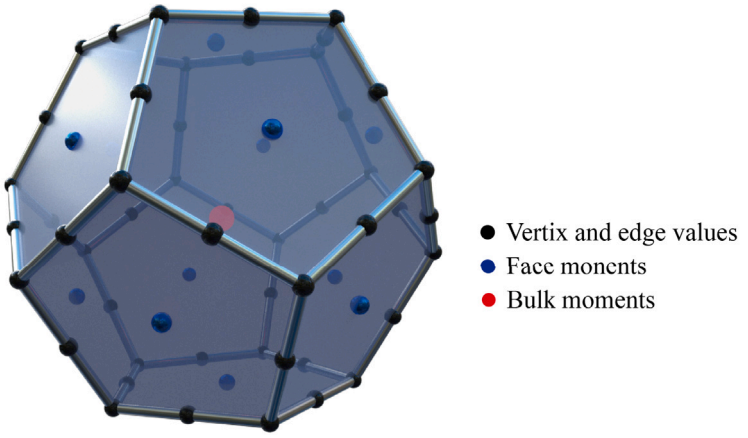

Fig. 3. Local degrees of freedom for $k = 2$.

Once the boundary space is defined, the preliminary local virtual element space on E can be defined as

$$\tilde{\mathcal{V}}_k(E) := \left\{ \boldsymbol{v} \in \boldsymbol{\mathcal{H}}_1 : \boldsymbol{v}|_{\partial E} \in \boldsymbol{\mathcal{B}}(\partial E), \Delta \boldsymbol{u} \in \left(\boldsymbol{\mathcal{P}}_{k-2}(E)\right)^3 \right\}. \tag{19}$$

Based on the definition of the boundary space and the preliminary local virtual element space, the associated degrees of freedom are given as

- the values of $\boldsymbol{v}_p$ at the vertices of E;
- the values of the $k-1$ internal Gauss–Lobatto nodes on each edge e of polyhedron E;
- moments on faces F of polyhedron E up to degree $k-2$

$$\frac{1}{|F|}\int_F \boldsymbol{v}\boldsymbol{p}^f_{k-2}\,\mathrm{d}\Omega_F, \quad \forall \boldsymbol{p}^f_{k-2} \in \boldsymbol{\mathcal{P}}_{k-2}(F), \quad \forall \text{face } F \in \partial E, \tag{20}$$

- bulk moments up to degree $k-2$

$$\frac{1}{|E|}\int_E \boldsymbol{v}\boldsymbol{p}_{k-2}\,\mathrm{d}\Omega, \quad \forall \boldsymbol{p}_{k-2} \in \boldsymbol{\mathcal{P}}_{k-2}(E). \tag{21}$$

For a given polyhedral element, the local degrees of freedom for $k = 2$ are depicted in Fig. 3.

The basic principle of the virtual element method is to define a projection Π^∇_k from the virtual element space to the polynomial space. The projection operator can be obtained based on the degrees of freedom of the element and the basis functions of the edges of the polygon (polyhedron) (interpolation functions for line elements are known).

As discussed in [9,13,15], for linear and nonlinear elastic problems, the displacement $\boldsymbol{u}_h$ can be split as $\Pi^\nabla_k \boldsymbol{u}_h$ and a remainder $\boldsymbol{u}_h - \Pi^\nabla_k \boldsymbol{u}_h$ as

$$\boldsymbol{u}_h = \Pi^\nabla_k \boldsymbol{u}_h + \left(\boldsymbol{u}_h - \Pi^\nabla_k \boldsymbol{u}_h\right), \tag{22}$$

where the vector projection operator Π^∇_k

$$\Pi^\nabla_k : \tilde{\mathcal{V}}_k(E) \to \left(\boldsymbol{\mathcal{P}}_k(E)\right)^3, \quad \boldsymbol{v} \mapsto \Pi^\nabla_k \boldsymbol{v}, \tag{23}$$

follows from

$$\begin{cases} \displaystyle\int_E \nabla \Pi^\nabla_k \boldsymbol{v} \cdot \nabla \boldsymbol{p}\,\mathrm{d}\Omega = \int_E \nabla \boldsymbol{v} \cdot \nabla \boldsymbol{p}\,\mathrm{d}\Omega, \quad \boldsymbol{p} \in \mathcal{P}_k(E) \\ \displaystyle\int_E \Pi^\nabla_k \boldsymbol{v}\,\mathrm{d}\Omega = \int_E \boldsymbol{v}\,\mathrm{d}\Omega \end{cases}. \tag{24}$$

Then we define the local virtual space as

$$\mathcal{V}_k(E) = \left\{ \boldsymbol{v} \in \tilde{\mathcal{V}}_k(E) : \int_E \boldsymbol{v} \cdot \boldsymbol{q}\,\mathrm{d}\Omega\,\mathrm{d}\Omega = \int_E \left(\Pi^\nabla_k \boldsymbol{v}\right) \cdot \boldsymbol{q}\,\mathrm{d}\Omega, \forall \boldsymbol{q} \in \boldsymbol{\mathcal{P}}_k \backslash \boldsymbol{\mathcal{P}}_{k-2} \right\}. \tag{25}$$

Inserting the basis functions $\boldsymbol{\phi}$ for the VEM space $\boldsymbol{\mathcal{V}}_k(E)$ and basis functions $\boldsymbol{m}$ for the polynomial space $\boldsymbol{\mathcal{P}}_k(E)$ in Eq. (24) yields

$$\begin{cases} \int_E \nabla \boldsymbol{m} \cdot \nabla \boldsymbol{\Pi}_k^{\nabla} \boldsymbol{\phi}^T \, \mathrm{d}\Omega = \int_E \nabla \boldsymbol{m} \cdot \nabla \boldsymbol{\phi}^T \, \mathrm{d}\Omega \\ \int_E \boldsymbol{\Pi}_k^{\nabla} \boldsymbol{\phi}^T \, \mathrm{d}\Omega = \int_E \boldsymbol{\phi}^T \, \mathrm{d}\Omega \end{cases}, \tag{26}$$

where the projection operator $\boldsymbol{\Pi}_k^{\nabla}$ can be expanded in a matrix form as

$$\boldsymbol{\Pi}_k^{\nabla} \boldsymbol{\phi}^T = \boldsymbol{m}^T \boldsymbol{\Pi}_{k*}^{\nabla} = \boldsymbol{\phi}^T \boldsymbol{\Pi}_k^{\nabla}, \tag{27}$$

here $\boldsymbol{\Pi}_{k*}^{\nabla}$ is matrix formulation of the Ritz projection operator.

Substituting Eq. (27) into Eq. (26) leads to the matrix form

$$\begin{cases} \boldsymbol{G} \boldsymbol{\Pi}_{k*}^{\nabla} = \boldsymbol{B} \\ \int_E \boldsymbol{m}^T \, \mathrm{d}\Omega \boldsymbol{\Pi}_{k*}^{\nabla} = \int_E \boldsymbol{\phi}^T \, \mathrm{d}\Omega \end{cases}, \tag{28}$$

where

$$\boldsymbol{G} = \int_E \nabla \boldsymbol{m} \cdot \nabla \boldsymbol{m}^T \, \mathrm{d}\Omega, \quad \boldsymbol{B} = \int_E \nabla \boldsymbol{m} \cdot \nabla \boldsymbol{\phi}^T \, \mathrm{d}\Omega. \tag{29}$$

Considering the Gaussian divergence theorem, the matrix $\boldsymbol{B}$ can be calculated by

$$\begin{aligned} \boldsymbol{B} &= \int_E \nabla \boldsymbol{m} \cdot \nabla \boldsymbol{\phi}^T \, \mathrm{d}\Omega \\ &= -\int_E \Delta \boldsymbol{m} \cdot \boldsymbol{\phi}^T \, \mathrm{d}\Omega + \sum_{F \subset \partial E} \int_F \left(\nabla \boldsymbol{m} \cdot \boldsymbol{n}_F \right) \boldsymbol{\phi}^T \, \mathrm{d}\Gamma \\ &= -\boldsymbol{I}_1 + \boldsymbol{I}_2, \end{aligned} \tag{30}$$

where

$$\boldsymbol{I}_1 = \int_E \Delta \boldsymbol{m} \cdot \boldsymbol{\phi}^T \, \mathrm{d}\Omega, \quad \boldsymbol{I}_2 = \sum_{F \subset \partial E} \int_F \left(\nabla \boldsymbol{m} \cdot \boldsymbol{n}_F \right) \boldsymbol{\phi}^T \, \mathrm{d}\Gamma. \tag{31}$$

Since $\Delta \boldsymbol{m} \in \mathcal{M}_{k-2}$ in $\boldsymbol{I}_1$, so that the integral can be computed exactly without knowing $\boldsymbol{v}$ in the interior of E, see Eq. (21). For evaluation of the second term $\boldsymbol{I}_2$, we define a local coordinate system for each face F (as shown in Fig. 2) and the elliptic projection $\boldsymbol{\Pi}_{k,F}^{\nabla}$ on the polygonal face can be obtained as

$$\begin{aligned} \boldsymbol{I}_2 &= \sum_{F \subset \partial E} \int_F \left(\nabla \boldsymbol{m} \cdot \boldsymbol{n}_F \right) \boldsymbol{\phi}^T \, \mathrm{d}\Gamma \\ &= \sum_{F \subset \partial E} \int_F \left(\nabla \boldsymbol{m} \cdot \boldsymbol{n}_F \right) \boldsymbol{\Pi}_{k,F}^{\nabla} \boldsymbol{\phi}^T \, \mathrm{d}\Gamma = \sum_{F \subset \partial E} \int_F \left(\nabla \boldsymbol{m} \cdot \boldsymbol{n}_F \right) \boldsymbol{m}_F^T \, \mathrm{d}\Gamma \boldsymbol{\Pi}_{k,F}^{\nabla}, \end{aligned} \tag{32}$$

where $\boldsymbol{\Pi}_{k,F}^{\nabla}$ is the local projection matrix for face F under the local coordinate as shown in Fig. 2. The calculation process of projection matrix $\boldsymbol{\Pi}_{k,F}^{\nabla}$ is similar to $\boldsymbol{\Pi}_k^{\nabla}$ in Eq. (28) and detailed in Appendix A. The integral in Eq. (32) can be calculated by dividing the polygon into triangles and utilizing the Gauss numerical integral method. Lastly, the matrix $\boldsymbol{B}$ can be calculated by

$$\boldsymbol{B} = -\boldsymbol{I}_1 + \boldsymbol{I}_2. \tag{33}$$

Compared with matrix $\boldsymbol{B}$, the calculation of matrix $\boldsymbol{G}$ is relatively simple. One way is to divide the polyhedron into tetrahedrons and then perform integration; another way is to define the matrix $\boldsymbol{D}$ as follows:

$$(\boldsymbol{D})_{i\alpha} := \mathrm{dof}_i(\boldsymbol{m}_\alpha), \tag{34}$$

where $\mathrm{dof}_i(\boldsymbol{m}_\alpha)$ is the ith degree of freedom of $\boldsymbol{m}_\alpha$ as given in Eqs. (20) and (21). Then, the matrix $\boldsymbol{G}$ can be calculated by

$$\boldsymbol{G} = \boldsymbol{B}\boldsymbol{D}. \tag{35}$$

For any given polyhedral element that meets the geometric requirements [56], the matrices $\boldsymbol{B}$ and $\boldsymbol{G}$ can be calculated and the Ritz projection matrix $\boldsymbol{\Pi}_{k*}^{\nabla}$ is obtained based on Eq. (28) and the projection matrix $\boldsymbol{\Pi}_k^{\nabla}$ follows as

$$\boldsymbol{\Pi}_k^{\nabla} = \boldsymbol{D} \boldsymbol{\Pi}_{k*}^{\nabla}. \tag{36}$$

4. Construction of the virtual element for elasticity

In the previous section, we derived the calculation process of projection operators for arbitrary order 3D VEM. For hyperelastic finite strain problems, we can perform calculations in the initial configuration. The related discretization process is similar to nonlinear finite element literature, see [57]. In addition, automatic differentiation is another powerful tool to obtain the residual and tangent stiffness matrix, see [58]. Next, we will briefly describe the specific format of the tangent stiffness matrix. The associated derivation process can be found in Appendix B.

4.1. Hyperelasticity

Considering the internal virtual work in a Lagrangian form as

$$\mathcal{W} = \int_{V_0} \delta \boldsymbol{E} : \boldsymbol{S} \, \mathrm{d}V_0, \tag{37}$$

the linearization of the virtual work is obtained as

$$\Delta\mathcal{W} = \int_{V_0} \delta \boldsymbol{E} : \Delta \boldsymbol{S} \, \mathrm{d}V_0 + \int_{V_0} \Delta(\delta \boldsymbol{E}) : \boldsymbol{S} \, \mathrm{d}V_0. \tag{38}$$

Utilization Voigt notation and considering the definition of the Green–Lagrange strain tensor $\boldsymbol{E}$ and $\Delta\hat{\boldsymbol{S}} = \hat{\boldsymbol{D}} : \Delta\hat{\boldsymbol{E}}$, the linearization of the virtual work follows as

$$\begin{aligned} \Delta\mathcal{W} &= \int_{V_0} \delta\hat{\boldsymbol{E}}^T \cdot \hat{\boldsymbol{D}} \cdot \Delta\hat{\boldsymbol{E}} \, \mathrm{d}V_0 + \int_{V_0} \delta\boldsymbol{\theta}^T \cdot \boldsymbol{\mathcal{I}} \cdot \Delta\boldsymbol{\theta} \, \mathrm{d}V_0 \\ &= \int_{V_0} \delta\boldsymbol{\theta}^T \cdot \left(\boldsymbol{A}^T \cdot \hat{\boldsymbol{D}} \cdot \boldsymbol{A} + \boldsymbol{\mathcal{I}} \right) \cdot \Delta\boldsymbol{\theta} \, \mathrm{d}V_0, \end{aligned} \tag{39}$$

where

$$\boldsymbol{\theta} = \left[\frac{\partial u}{\partial X} \quad \frac{\partial u}{\partial Y} \quad \frac{\partial u}{\partial Z} \quad \frac{\partial v}{\partial X} \quad \frac{\partial v}{\partial Y} \quad \frac{\partial v}{\partial Z} \quad \frac{\partial w}{\partial X} \quad \frac{\partial w}{\partial Y} \quad \frac{\partial w}{\partial Z} \right]^T, \tag{40}$$

and $\hat{\boldsymbol{E}} = \boldsymbol{A} \cdot \boldsymbol{\theta}$, $\delta\hat{\boldsymbol{E}} = \boldsymbol{A} \cdot \delta\boldsymbol{\theta}$, $\Delta\hat{\boldsymbol{E}} = \boldsymbol{A} \cdot \Delta\boldsymbol{\theta}$. Besides, the constitutive tensor $\hat{\boldsymbol{D}}$ can be obtained based on the strain energy density function Ψ, see Eqs. (11) and (14). The specific format of tensor $\boldsymbol{\mathcal{I}}$ and $\boldsymbol{A}$ can be found in Appendix B.

Considering the projection matrix $\boldsymbol{\Pi}_k^{\nabla}$ we solved from Eqs. (28) and (36) for any given 3D polyhedral element, we have

$$\Delta\boldsymbol{\theta} \doteq \nabla\boldsymbol{\phi}^T \cdot \boldsymbol{\Pi}_k^{\nabla} \cdot \Delta\boldsymbol{U} = \nabla\boldsymbol{m}^T \cdot \boldsymbol{\Pi}_{k*}^{\nabla} \cdot \Delta\boldsymbol{U}, \tag{41}$$

where $\boldsymbol{U}$ is a vector composed of the degrees of freedom in the polyhedral element and $\Delta\boldsymbol{U}$ is the increment. We should note that Eq. (41) is not strictly equal and we use $\doteq$ since only the projection part is considered.

As shown in Eq. (22) and some previous references, the displacement is divided into a projection part and a remainder, so additional stabilization terms are needed in the VEM to ensure the correct rank of the tangent stiffness matrix. Considering Eq. (22) in Eq. (41), we have

$$\begin{aligned} \Delta\boldsymbol{\theta} &= \nabla\boldsymbol{\phi}^T \cdot \boldsymbol{\Pi}_k^{\nabla} \cdot \Delta\boldsymbol{U} + \left(\Delta\boldsymbol{\theta} - \nabla\boldsymbol{\phi}^T \cdot \boldsymbol{\Pi}_k^{\nabla} \cdot \Delta\boldsymbol{U} \right) \\ &= \nabla\boldsymbol{m}^T \cdot \boldsymbol{\Pi}_{k*}^{\nabla} \cdot \Delta\boldsymbol{U} + \nabla\boldsymbol{\phi}^T \cdot \left(\boldsymbol{I}_K - \boldsymbol{\Pi}_k^{\nabla} \right) \cdot \Delta\boldsymbol{U}, \end{aligned} \tag{42}$$

where $\boldsymbol{I}_K$ is an identity matrix that has the same size as the $\boldsymbol{\Pi}_k^{\nabla}$. Substituting Eq. (42) into Eq. (39), the linearization of the virtual work becomes

$$\begin{aligned} \Delta\mathcal{W} =& \delta\boldsymbol{U}^T \cdot \left(\boldsymbol{\Pi}_{k*}^{\nabla} \right)^T \cdot \int_{V_0} \nabla\boldsymbol{m} \left(\boldsymbol{A}^T \cdot \hat{\boldsymbol{D}} \cdot \boldsymbol{A} + \boldsymbol{\mathcal{I}} \right) \nabla\boldsymbol{m}^T \, \mathrm{d}V_0 \cdot \boldsymbol{\Pi}_{k*}^{\nabla} \cdot \Delta\boldsymbol{U} \\ &+ \delta\boldsymbol{U}^T \cdot \left(\boldsymbol{I}_K - \boldsymbol{\Pi}_k^{\nabla} \right)^T \cdot \int_{V_0} \nabla\boldsymbol{\phi} \left(\boldsymbol{A}^T \cdot \hat{\boldsymbol{D}} \cdot \boldsymbol{A} + \boldsymbol{\mathcal{I}} \right) \nabla\boldsymbol{\phi}^T \, \mathrm{d}V_0 \cdot \left(\boldsymbol{I}_K - \boldsymbol{\Pi}_k^{\nabla} \right) \cdot \Delta\boldsymbol{U}. \end{aligned} \tag{43}$$

Based on Eq. (43), the element tangent stiffness matrix can be obtained as

$$\boldsymbol{K}^{NL} = \boldsymbol{K}_c^{NL} + \boldsymbol{K}_s^{NL}, \tag{44}$$

where $\boldsymbol{K}_s^{NL}$ is the consistency term and $\boldsymbol{K}_s^{NL}$ is the stabilization term. The specific form can be derived from Eq. (43) as

$$\boldsymbol{K}_c^{NL} = \left(\boldsymbol{\Pi}_{k*}^{\nabla} \right)^T \cdot \int_{V_0} \nabla\boldsymbol{m} \left(\boldsymbol{A}^T \cdot \hat{\boldsymbol{D}} \cdot \boldsymbol{A} + \boldsymbol{\mathcal{I}} \right) \nabla\boldsymbol{m}^T \, \mathrm{d}V_0 \cdot \boldsymbol{\Pi}_{k*}^{\nabla}, \tag{45}$$

and

$$\boldsymbol{K}_s^{NL} = \left(\boldsymbol{I}_K - \boldsymbol{\Pi}_k^{\nabla} \right)^T \cdot \int_{V_0} \nabla\boldsymbol{\phi} \left(\boldsymbol{A}^T \cdot \hat{\boldsymbol{D}} \cdot \boldsymbol{A} + \boldsymbol{\mathcal{I}} \right) \nabla\boldsymbol{\phi}^T \, \mathrm{d}V_0 \cdot \left(\boldsymbol{I}_K - \boldsymbol{\Pi}_k^{\nabla} \right). \tag{46}$$

Considering $\int_{V_0} \nabla\phi\nabla\phi^T \approx \mathcal{O}(1)$ (under suitable mesh regularity assumptions), the stabilization matrix can be approximated as

$$\boldsymbol{K}_s^{NL} = \alpha \left(\boldsymbol{I}_K - \boldsymbol{\Pi}_k^{\nabla} \right)^T \left(\boldsymbol{I}_K - \boldsymbol{\Pi}_k^{\nabla} \right), \tag{47}$$

where α is a stabilization parameter, which depends on different material constants (also nonlinear materials).

There are some discussions on the stabilization parameter α for hyperelastic problems in first-order VEM, see [9,18,21,59]. As described in Ref. [18], the authors provided two different stabilization techniques, including norm-based stabilization and trace-based stabilization. In this work, for hyperelastic problems, considering the trace of constitutive tangent, the stabilization parameter α for second-order 3D VEM is selected as

$$\alpha = \frac{1}{d^2} \mathrm{tr}\left(\hat{\boldsymbol{D}} \right) = \frac{4}{9} \mathrm{tr}\left(\frac{\partial^2 \Psi}{\partial \boldsymbol{C} \partial \boldsymbol{C}} \right), d = 3, \tag{48}$$

and thus depends on the deformation state. Of course, there are many other ways to choose the stabilization parameters, such as non-linear stabilization in [9,21,26].

The internal force is obtained based on Eq. (37):

$$\delta \boldsymbol{U}^T \cdot \boldsymbol{F}_{\text{int}} = \int_{V_0} \delta \hat{\boldsymbol{E}}^T \cdot \hat{\boldsymbol{S}} \, \mathrm{d}V_0 = \int_{V_0} (\boldsymbol{A} \cdot \delta \boldsymbol{\theta})^T \cdot \hat{\boldsymbol{S}} \, \mathrm{d}V_0. \tag{49}$$

With Eq. (22), the internal force can be formulated as

$$\boldsymbol{F}_{\text{int}} = \left(\boldsymbol{\Pi}_{k*}^{\nabla}\right)^T \cdot \int_{V_0} \nabla \boldsymbol{m} \cdot \boldsymbol{A}^T \cdot \hat{\boldsymbol{S}} \, \mathrm{d}V_0 + \boldsymbol{F}_{\text{int}}^s, \tag{50}$$

where $\boldsymbol{F}_{\text{int}}^s$ is the stabilization term for internal force, which can be approximated by

$$\boldsymbol{F}_{\text{int}}^s = \boldsymbol{K}_s^{NL} \cdot \boldsymbol{U}. \tag{51}$$

4.2. Linear elasticity

Considering the Saint Venant–Kirchhoff model and the small deformation assumption, the stiffness matrix format of the linear elastic problem is

$$\boldsymbol{K}^L = \boldsymbol{K}_c^L + \boldsymbol{K}_s^L, \tag{52}$$

with

$$\boldsymbol{K}_c^L = \left(\boldsymbol{\Pi}_{k*}^{\nabla}\right)^T \cdot \int_{V_0} \nabla \boldsymbol{m} \cdot \tilde{\boldsymbol{A}}^T \cdot \hat{\boldsymbol{D}} \cdot \tilde{\boldsymbol{A}} \cdot \nabla \boldsymbol{m}^T \, \mathrm{d}V_0 \cdot \boldsymbol{\Pi}_{k*}^{\nabla}, \tag{53}$$

where the matrix $\tilde{\boldsymbol{A}}$ is given in Appendix B. Besides, the stabilization matrix can be approximated as

$$\boldsymbol{K}_s^L = \alpha \left(\boldsymbol{I}_K - \boldsymbol{\Pi}_k^{\nabla}\right)^T \left(\boldsymbol{I}_K - \boldsymbol{\Pi}_k^{\nabla}\right), \tag{54}$$

and α is a stabilization parameter, which can be selected with a similar form as given in Eq. (48), $\alpha = \frac{1}{9}\mathrm{tr}(\hat{\boldsymbol{D}})$ with for linear elasticity is constant.

4.3. Stresses and internal force

For linear elasticity, once we have solved the displacement vector $\boldsymbol{U}$, we can proceed to calculate the strains and stresses as

$$\hat{\varepsilon} = \tilde{\boldsymbol{A}} \nabla \boldsymbol{m}^T \boldsymbol{\Pi}_{k*}^{\nabla} \boldsymbol{U}, \quad \hat{\boldsymbol{\sigma}} = \hat{\boldsymbol{D}} \hat{\varepsilon} = \hat{\boldsymbol{D}} \tilde{\boldsymbol{A}} \nabla \boldsymbol{m}^T \boldsymbol{\Pi}_{k*}^{\nabla} \boldsymbol{U}. \tag{55}$$

For finite strain elasticity, we should calculate the deformation gradient $\boldsymbol{F}$ and then the right Cauchy–Green tensor $\boldsymbol{C}$ in each iteration. The deformation gradient $\boldsymbol{F}$ can be calculated by

$$\boldsymbol{F} = \boldsymbol{I} + \nabla \boldsymbol{m}^T \boldsymbol{\Pi}_{k*}^{\nabla} \boldsymbol{U}_t, \tag{56}$$

where $\boldsymbol{U}_t$ is the displacement at current step. We can calculate the Piola–Kirchhoff stress $\boldsymbol{S}$ based on Eq. (15), and the Cauchy stress $\boldsymbol{\sigma}$ can be calculated as

$$\boldsymbol{\sigma} = \frac{1}{\boldsymbol{J}} \boldsymbol{F} \boldsymbol{S} \boldsymbol{F}^T \tag{57}$$

For hyperelastic problems, the internal force can be obtained based on Eq. (37):

$$\delta \boldsymbol{U}^T \cdot \boldsymbol{F}_{\text{int}} = \int_{V_0} \delta \hat{\boldsymbol{E}}^T \cdot \hat{\boldsymbol{S}} \, \mathrm{d}V_0 = \int_{V_0} (\boldsymbol{A} \cdot \delta \boldsymbol{\theta})^T \cdot \hat{\boldsymbol{S}} \, \mathrm{d}V_0. \tag{58}$$

Based on Eq. (22), the internal force can be obtained as

$$\boldsymbol{F}_{\text{int}} = \left(\boldsymbol{\Pi}_{k*}^{\nabla}\right)^T \cdot \int_{V_0} \nabla \boldsymbol{m} \cdot \boldsymbol{A}^T \cdot \hat{\boldsymbol{S}} \, \mathrm{d}V_0 + \boldsymbol{F}_{\text{int}}^s, \tag{59}$$

where $\boldsymbol{F}_{\text{int}}^s$ is the stabilization term for internal force, which can be approximated by

$$\boldsymbol{F}_{\text{int}}^s = \boldsymbol{K}_s^{NL} \cdot \boldsymbol{U}_t. \tag{60}$$

5. Numerical examples

5.1. 3D Cook's membrane problem

In the first example, the 3D Cook's membrane problem is considered to assess the bending behavior of the proposed method. The cantilever beam is fixed on the left side, and tractions are applied at the right side for two cases: $T_1 = (0, f, 0)$ and $T_2 = (0, 2f, f)$. The geometric dimensions are $H_1 = 44$, $H_2 = 16$, $L = 48$, and $B = 10$ (shown in Fig. 4). The problem will be analyzed using the assumptions of small and large deformations, respectively.

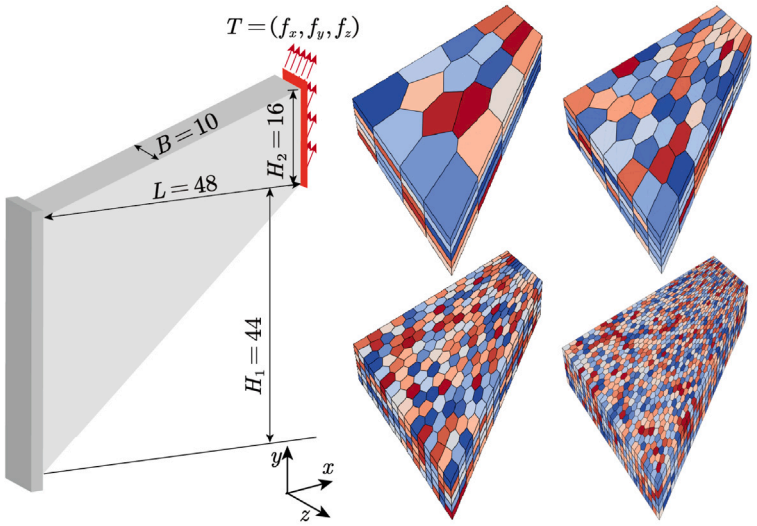

Fig. 4. 3D Cook's membrane: Geometry and meshes.

Table 1
Maximum displacements u_y for different discretizations under T_1.

N	VEM		FEM	
	$k=1$	$k=2$	$k=1$(Q1)	$k=2$(Q2)
2	0.647014	0.788781	0.573815	0.778637
3	0.735537	0.794386	0.712435	0.791497
4	0.776021	0.797581	0.768878	0.796696
5	0.790484	0.799169	0.788673	0.798904

Table 2
Maximum total displacements u_{sum} for different discretizations under T_2.

N	VEM		FEM	
	$k=1$	$k=2$	$k=1$(Q1)	$k=2$(Q2)
2	4.59913	7.34473	3.77858	7.25192
3	5.69291	7.37835	5.86101	7.34340
4	6.34573	7.38426	6.88095	7.37632
5	6.55272	7.39121	7.21377	7.38967

5.1.1. Linear elasticity analysis

A linear elastic analysis of the Cook's membrane is performed under the assumption of small deformations. The material parameters with $E = 10$ and $\nu = 0.3$ are given. To verify the accuracy and convergence of the higher-order VEM in this problem, four different mesh discretizations are described with the parameter N. By selecting $N = 2, 3, 4, 5$, such that the element is divided into $2N \times 2N$ in the vertical and horizontal directions (see Fig. 4). A first-order VEM and the finite element method with linear and quadratic ansatz functions (Q1 and Q2) are used for comparison.

Firstly, the traction force T_1 with $f = 0.02$ ($T_1 = (0, f, 0)$) is applied at the right side. The maximum vertical displacement values obtained from the calculations for different element divisions are listed in Table 1. Fig. 5(a) shows the convergence analysis for the maximum displacement u_y. It can be seen that the computational results of the higher-order VEM are similar to those of the higher-order FEM, and both exhibit good computational accuracy and convergence speed. In addition, the higher-order methods can achieve greater computational accuracy when compared with the first-order methods.

Secondly, the traction force T_2 with $f = 0.02$ ($T_2 = (0, 2f, f)$) is used for the three-dimensional deformation of Cook's membrane. Table 2 lists the total displacement values for the different element divisions under traction force T_2. The convergence analysis of the total displacement u_{sum} is shown in Fig. 5(b). It can be seen that the higher-order VEM achieves better accuracy and convergence speed, while the convergence of the first-order VEM for displacements under load T_2 is quite slow.

For two different loading forms and different meshes, the obtained results by high-order VEM for displacement and stress are plotted in Fig. 6 and Fig. 7, respectively.

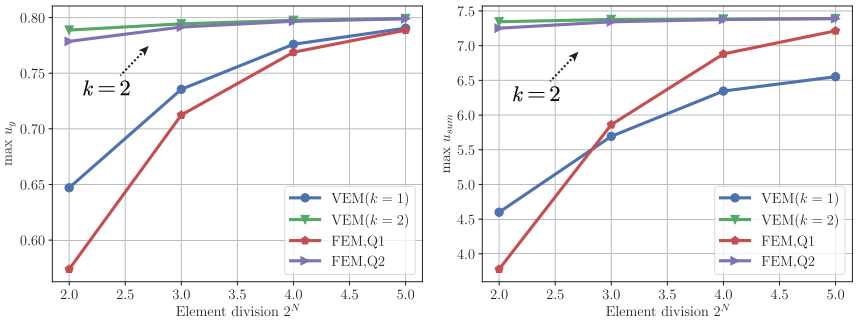

(a) T_1 with $f=0.02$ (b) T_2 with $f=0.02$

Fig. 5. Displacement obtained by different discretizations under different methods; (a) vertical displacement for T_1; (b) real displacement for T_2.

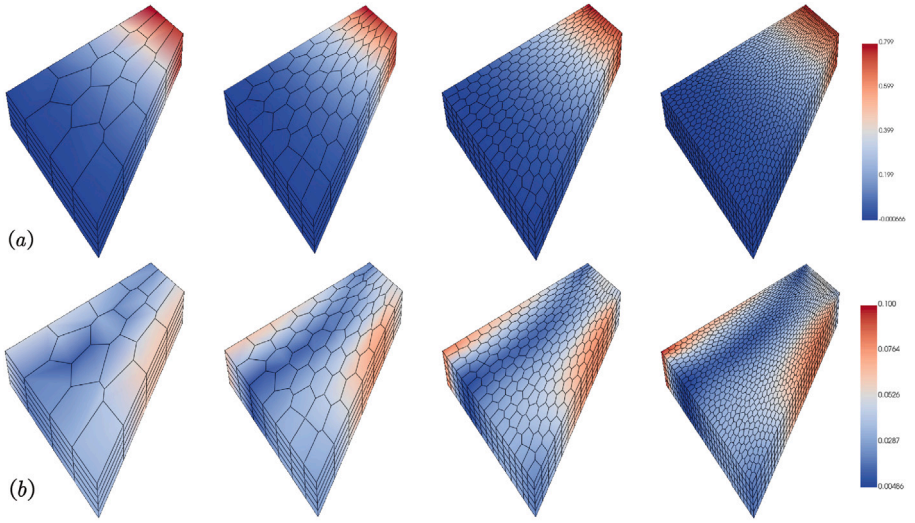

Fig. 6. Contour plots for different meshes under the traction force $T_1 = (0, 0.02, 0)$; (a) displacement u_y; (b) von Mises stresses.

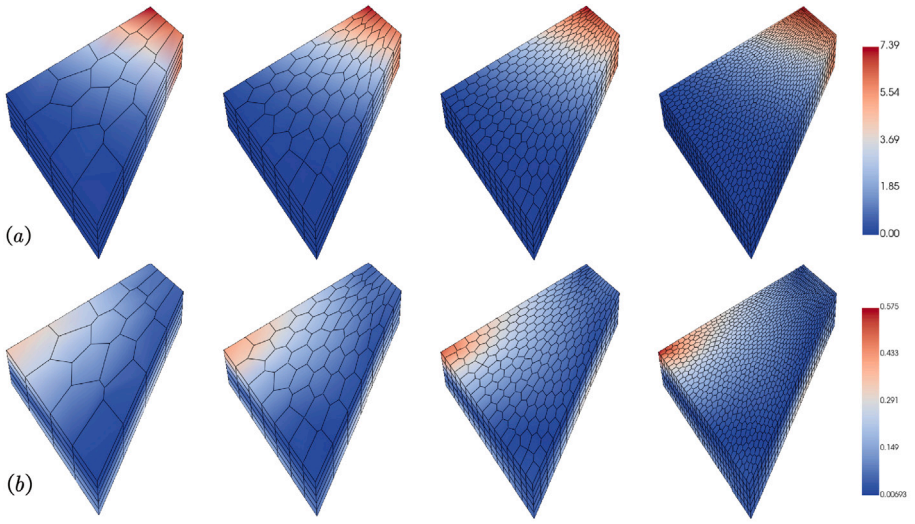

Fig. 7. Contour plots for different meshes under the traction force $T_2 = (0, 0.04, 0.02)$; (a) displacement u_{sum}; (b) von Mises stresses.

Table 3
Maximum displacements u_y for different discretizations under $T_1 = (0, 4, 0)$.

N	VEM		FEM	
	$k = 1$	$k = 2$	$k = 1$(Q1)	$k = 2$(Q2)
2	9.6363	11.2741	8.62856	11.162
3	10.7117	11.2943	10.3517	11.2515
4	11.0981	11.2943	11.0072	11.2828
5	11.2351	11.3027	11.2099	11.2974

Table 4
Maximum total displacements u_{sum} for different discretizations under $T_2 = (0, 6, 3)$.

N	VEM		FEM	
	$k = 1$	$k = 2$	$k = 1$(Q1)	$k = 2$(Q2)
2	30.4996	34.9161	27.7125	35.0333
3	33.001	35.3562	32.7994	35.352
4	33.9804	35.4346	34.543	35.436
5	34.2571	35.469	35.0847	35.4734

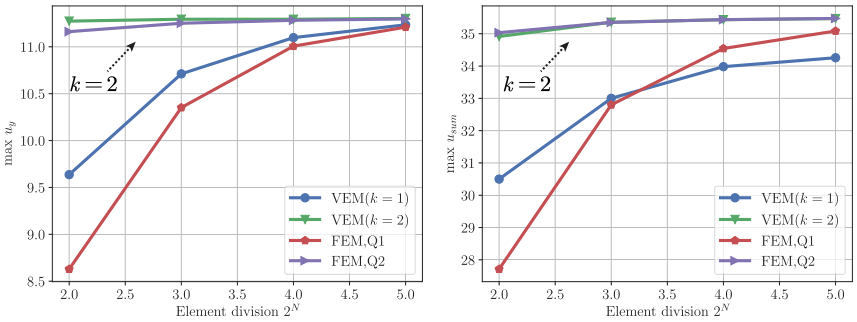

$(a) T_1$ with $f = 4$ $(b) T_2$ with $f = 3$

Fig. 8. Displacement obtained by different discretizations for different methods; (a) vertical displacement for $T_1 = (0, 4, 0)$; (b) total displacement for $T_2 = (0, 6, 3)$.

5.1.2. Nonlinear elasticity analysis

Finite strain elasticity is considered for Cook's membrane using a Neo-Hookean model with material parameters $\lambda = 100$ and $\nu = 40$. To verify the accuracy and convergence of the higher-order VEM in such hyperelastic materials, the same element divisions as in linear elastic analysis are chosen. The results obtained from the first-order VEM and the finite element method are still selected for comparison.

For the first loading condition, the right-hand traction force $T_1 = (0, f, 0)$ is applied with $f = 4$. The calculated maximum vertical displacement u_y for different element divisions is listed in Table 3. Fig. 8(a) shows the convergence analysis of the maximum displacement u_y. The second-order VEM continues to demonstrate high computational accuracy in problems involving finite deformation.

For the second loading condition, $T_2 = (0, 2f, f)$ with $f = 3$ is chosen as the right-hand side traction force. The values and convergence analysis of the maximum real displacements for different element divisions are shown in Table 4 and Fig. 8(b), respectively. Again the convergence of the first-order VEM is not good for the given traction force T_2. On the contrary, the higher-order VEM still produces highly accurate results similar to those of the higher-order FEM.

The deformation configurations and the displacements u_y and von Mises stress contour plots for the different meshes under the traction force T_1 are depicted in Fig. 9. Meanwhile, Fig. 10 shows the deformations and the contours of the different meshes under the traction force T_2.

5.2. Punch problem

The second example considers a block under a vertical uniform load. The geometry and dimensions are shown in Fig. 11, where $L_1 = L_2 = 2$ and $H = 1$. The Neo-Hookean material model is used with the Lame constants $\lambda = 400.75$ and $\mu = 92.5$. A uniform load of $P_1 = 300$ and $P_2 = 600$ is applied to the upper surface and the other boundary conditions are shown in Fig. 11.

As in the previous example, the discretized mesh of different scales is described by the parameter N. The model is divided into $N \times 2N \times 2N$ equivalent meshes with $N = 4, 6, 8, 10$, and 16. The first-order finite element method (FEM, Q1) and second-order finite element method (FEM, Q2) are used for comparison. The vertical displacement u_z of point A (as shown in Fig. 11) is selected for convergence analysis in different meshes.

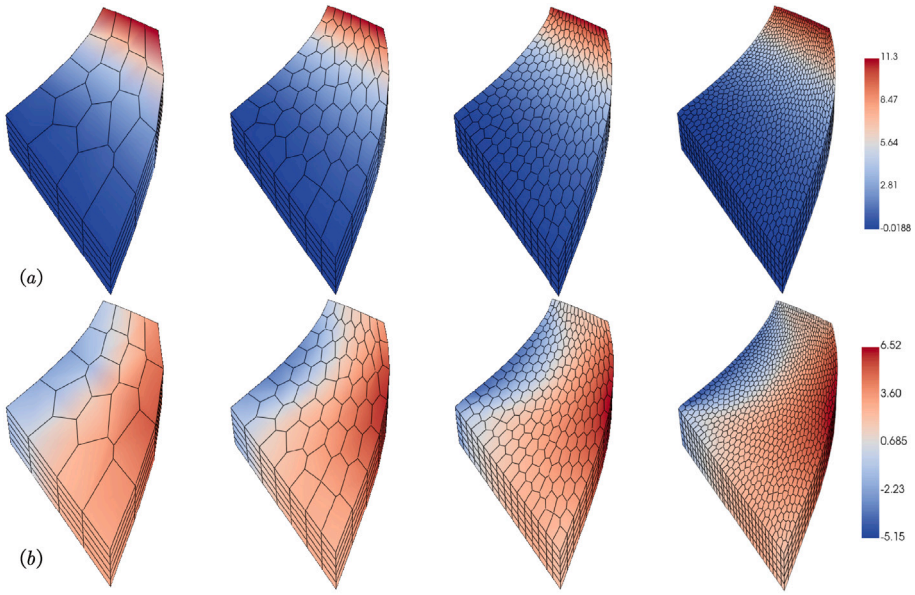

Fig. 9. Contour plots for different meshes under the traction force $T_1 = (0, 4, 0)$; (a) displacement u_y; (b) stresses s_{xy}.

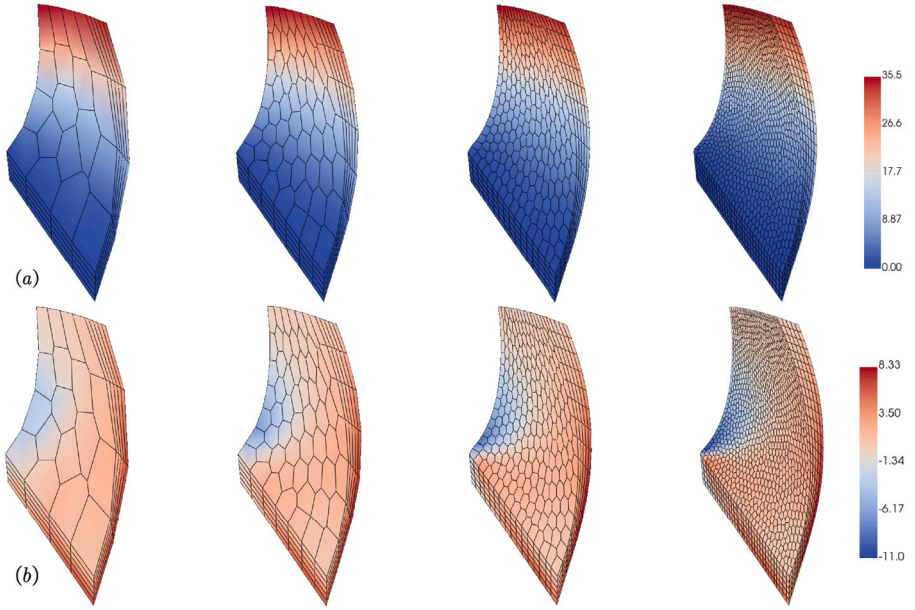

Fig. 10. Contour plots for different meshes under the traction force $T_2 = (0, 6, 3)$; (a) displacement u_{sum}; (b) stresses s_{xy}.

The values of the vertical displacement u_z at point A are listed in Table 5 for both the regular and polyhedral meshes of the high-order VEM while the pressure at the top is $P = P_1 = 300$. The convergence of the displacements u_z at point A for different methods under the current pressure load is shown in Fig. 12(a). It can be observed that even with the coarse meshes, the second-order VEM is capable of achieving more accurate results. The results obtained by second-order VEM using the regular hexahedral mesh are found to be in close agreement with those obtained by second-order FEM.

Besides, a pressure of value $P_2 = 600$ is applied to the top of the block, and the convergence analysis of the vertical displacement at point A obtained for different meshes is given in Table 6 and illustrated in Fig. 12(b). Even though the block is under strong pressure, the second-order VEM can yield accurate and stable results. In contrast, the first-order VEM exhibits poor convergence in this problem, regardless of whether the pressure is P_1 or P_2.

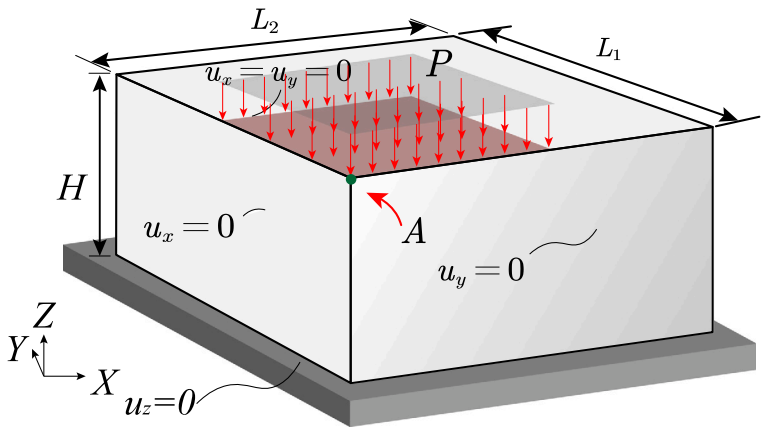

Fig. 11. Block under compression: Geometry and boundary conditions.

Table 5
The vertical displacement u_z of point A for different element divisions N under P_1.

N	VEM(regular)		VEM(polyhedral)		FEM	
	$k = 1$	$k = 2$	$k = 1$	$k = 2$	$k = 1$(Q1)	$k = 2$(Q2)
4	−0.4570	−0.6343	−0.4482	−0.6333	−0.6555	−0.6352
6	−0.4828	−0.6358	−0.4747	−0.6384	−0.6449	−0.6345
8	−0.5003	−0.6353	−0.4929	−0.6380	−0.6403	−0.6344
10	−0.5132	−0.6349	−0.5064	−0.6379	−0.6382	−0.6344
16	−0.5383	−0.6345	−0.5330	−0.6351	−0.6358	−0.6344

Table 6
The vertical displacement u_z of point A for different element divisions N under P_2.

N	VEM(regular)		VEM(polyhedral)		FEM	
	$k = 1$	$k = 2$	$k = 1$	$k = 2$	$k = 1$(Q1)	$k = 2$(Q2)
4	−0.5755	−0.7888	−0.5675	−0.7847	−0.869	−0.8063
6	−0.5989	−0.7958	−0.5908	−0.7919	−0.8441	−0.8045
8	−0.6152	−0.7996	−0.6065	−0.8013	−0.8265	−0.8045
10	−0.6275	−0.8015	−0.6191	−0.8036	−0.8174	−0.8045
16	−0.6522	−0.8031	−0.6446	−0.804	−0.8084	−0.8045

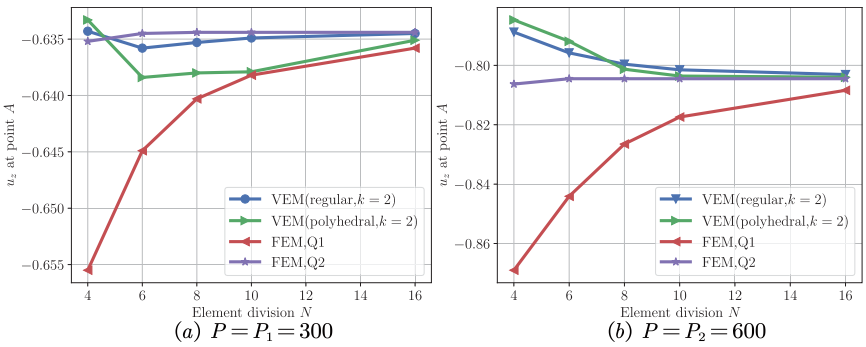

Fig. 12. The vertical displacement u_z of point A for different element division N:(a) for $P = P_1 = 300$; (b) for $P = P_2 = 600$.

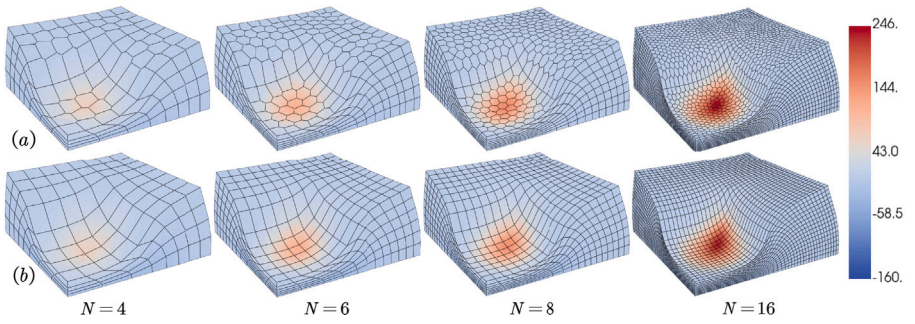

Fig. 13. Contour plots of stress S_{xy} obtained by second-order VEM with different meshes under pressure P_2.

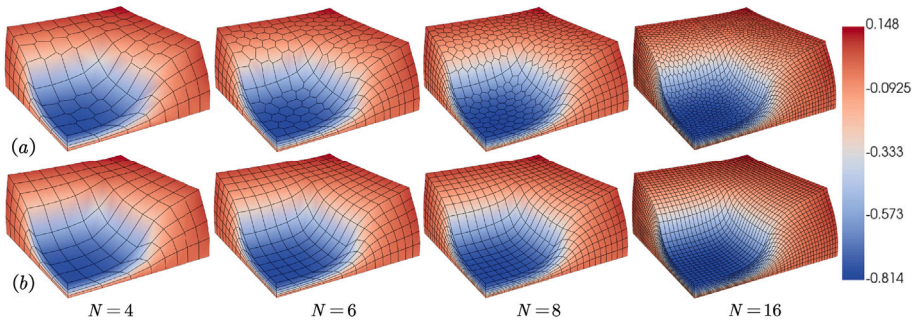

Fig. 14. Deformed shape and the vertical displacement contours obtained by second-order VEM with different meshes under pressure P_2.

Finally, the contour plots of stress S_{xy} obtained by the second-order VEM on the hexahedral mesh and polyhedral mesh for a pressure of P_2 are depicted in Fig. 13. Fig. 14 shows the contour plots of displacement u_z obtained by the second-order VEM on the hexahedral mesh for larger pressures P_2.

5.3. Three-dimensional fracture mechanics with non-matching mesh

To get more accurate stress results for a lot of fracture mechanical problems, denser meshes are often needed near the crack surface. In the traditional finite element method, it is relatively complicated to generate pure hexahedral meshes with local refinement. Since the virtual element method can automatically handle polyhedral meshes, the "hanging nodes" in the finite element method can be consistently adapted in VEM. Therefore, the virtual element method can directly pre-refine the mesh in a specified area without affecting the global mesh.

In this work, a cylindrical tube with a through-crack (shown in Fig. 15) is considered under the small strain assumption. The inner radius of the cylinder is 9, the outer radius is 10, and the overall length is 40. Given the symmetry of the model, only the 1/4 model is selected for calculation (see Fig. 15(b)). As shown in Fig. 16, we use smaller-sized elements for discretization (can be hexahedrons or polyhedrons) near the crack surface. In the process of transition between elements of different sizes, we directly use VEM to handle the hanging nodes existing in the model, thereby avoiding discontinuous displacements or the introduction of other interpolation techniques.

The material parameters are assumed as $E = 200000$ and $\nu = 0.3$. In addition, both ends of the cylindrical tube are subject to a uniformly distributed load $P = -1000$ (negative sign means the load is outward). Furthermore, the second-order finite element method (FEM, Q2) with a fine mesh is chosen for comparison. To facilitate comparison with the finite element results, we define a path (path 1) as shown in Fig. 15. The comparison of the displacement and stress results obtained by high-order VEM and the finite element method on path 1 are shown in Fig. 17. It can be seen that the displacement results calculated by VEM are very accurate and the stress results are within the acceptable range. Lastly, the contour plots of von Mises stress for different meshes are given in Fig. 18

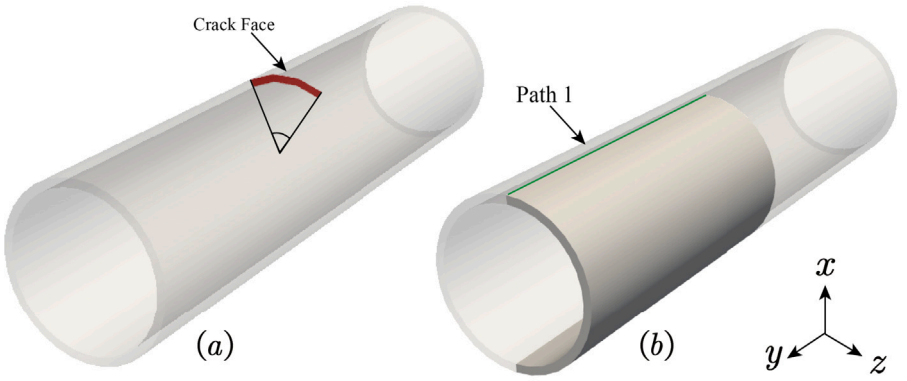

Fig. 15. Cylindrical tube with through-crack, (a) geometric model and crack surface, (b) 1/4 model used for calculation.

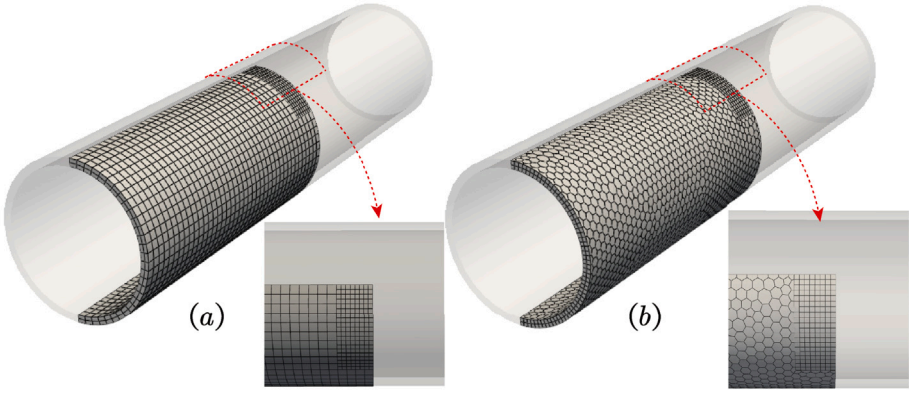

Fig. 16. Non-matching meshes for the cylindrical tube (a) hexahedron-dominated mesh, (b) polyhedron-dominated mesh.

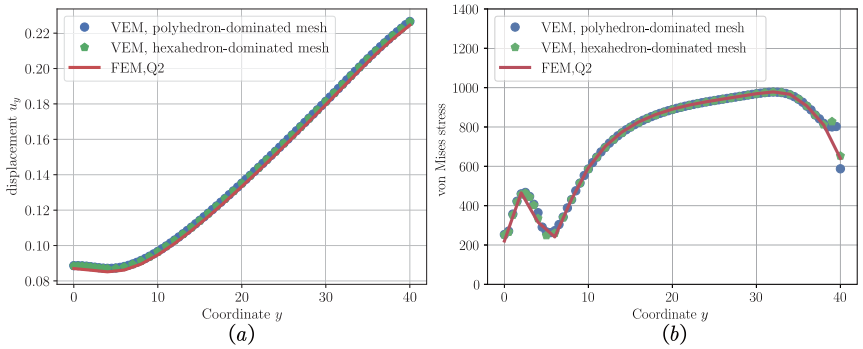

Fig. 17. Numerical solutions of displacement and stress on path 1 obtained by VEM ($k = 2$),(a) displacement u_y, (b) von Mises stress.

5.4. Torsion of a specimen with finite strain

Torsion problems can be used to test the effect of extreme mesh distortion during the deformation process. As shown in Fig. 19, two different geometric models are selected for the analysis of this example. The first structure is a square column with size $L \times D \times H = 1 \times 1 \times 10$ (see Fig. 19(a)). The second structure is a square column with bifurcation (see Fig. 19(b))[1]

In this example, the polyhedral mesh and finite element mesh (hexahedral mesh) are employed for the two structures respectively, as shown in Fig. 19. For the first square column, the bottom nodes are fixed and the top nodes rotate around the Z-axis. For the

[1] The geometry file given in https://github.com/Qinxiaoye/geometry/blob/main/torsion.stp.

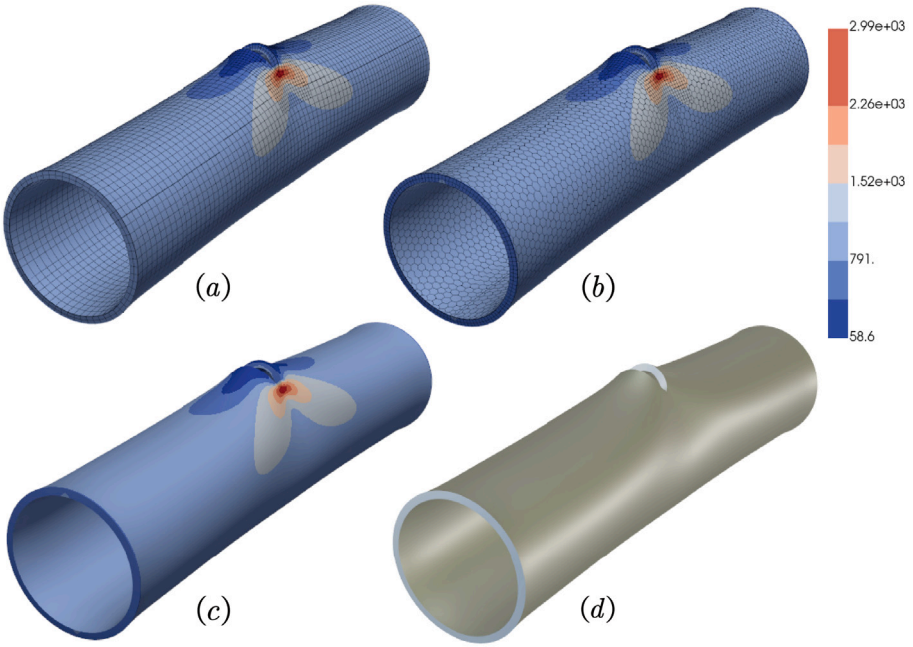

Fig. 18. Contour plots of von Mises stress for different meshes (scale factor is 20), (a) hexahedron-dominated mesh, (b) polyhedron-dominated mesh, (c) polyhedron-dominated mesh without edge, (d) structure after deformation.

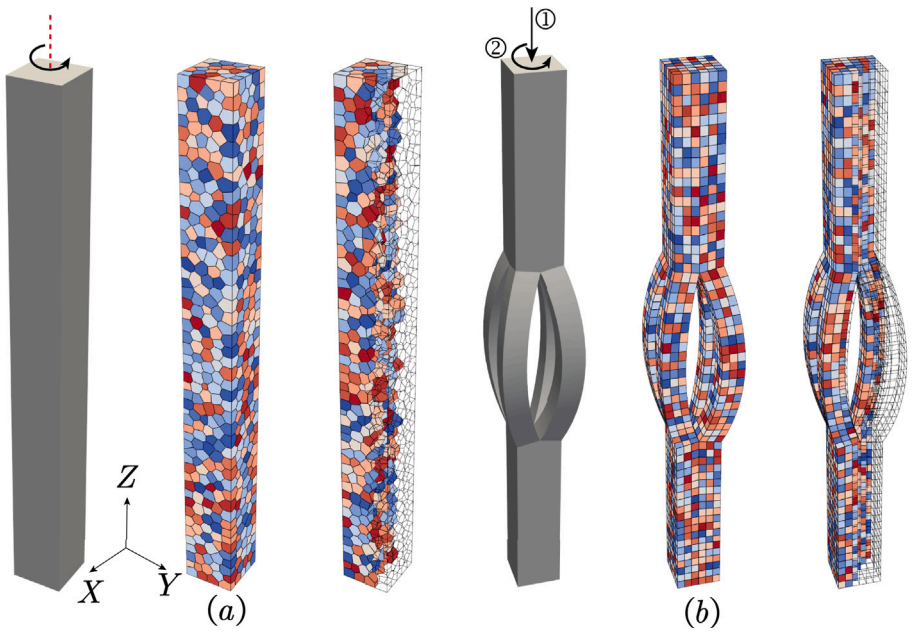

Fig. 19. Geometries and meshes for hyperelastic torsion, (a) square column, (b) square column with bifurcation.

second square column with bifurcation, the bottom nodes are fixed and the analysis process consists of two sub-steps: the first step: a displacement ($u_z = -1$) is applied at the nodes on the top; in the second step: the nodes are fixed and rotated around the Z-axis at the top. The material model for the two geometries is assumed as the Neo-Hookean hyperelastic law with the Lame parameters $\lambda = 100$ and $\mu = 40$.

For the first square column, the deformed meshes and contour plots of displacement u_x are given in Fig. 20 for different rotation angles. The expected twisting deformations are depicted in Fig. 20. It is also noticeable a warping deformation along the column is observed for $\theta = \frac{20}{3}\pi$, which indicates that the numerical solutions are still converging to the correct physical behavior. For the

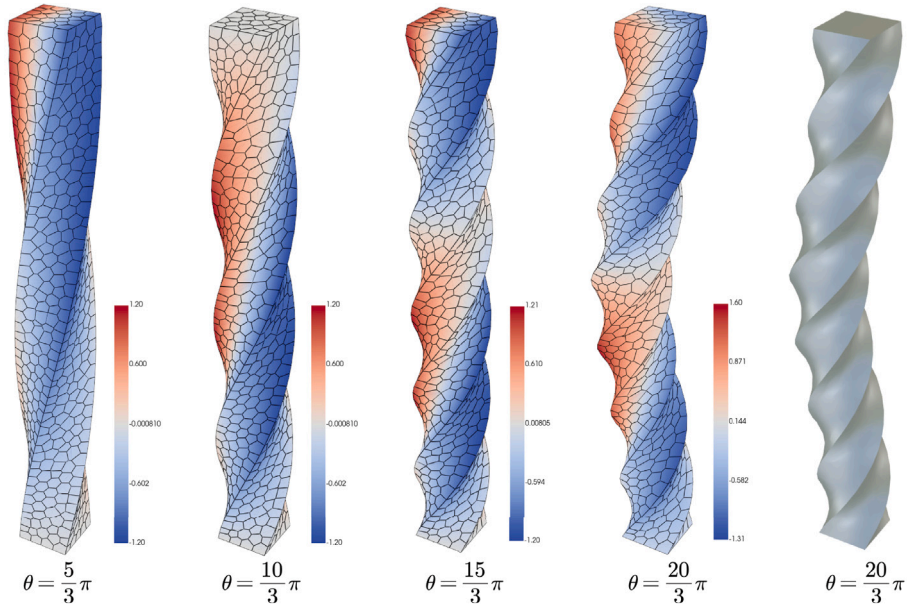

Fig. 20. Contour plots of displacement u_x obtained by VEM ($k = 2$) for the square column.

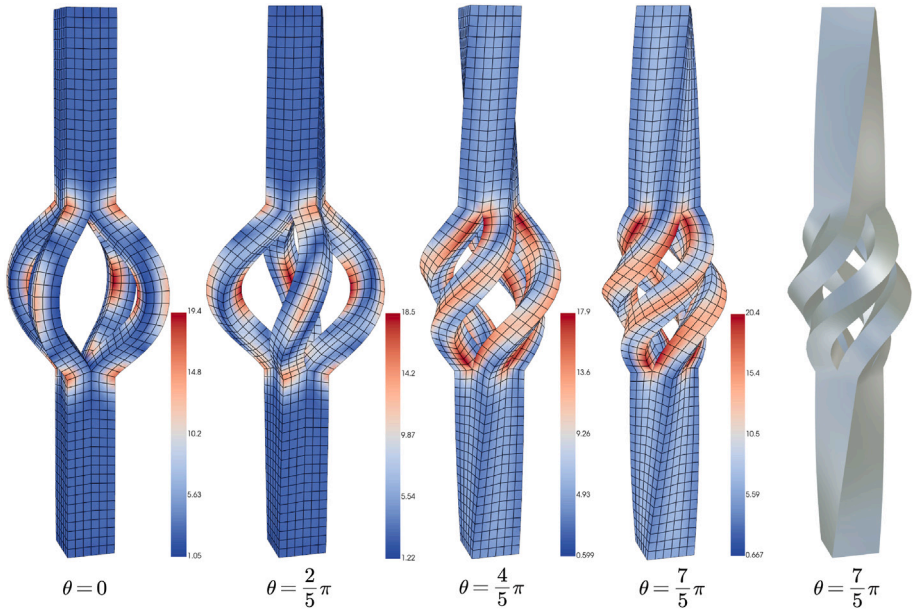

Fig. 21. Contour plots of von Mises stress obtained by VEM ($k = 2$) for the square column with bifurcation.

second square column (square column with bifurcation), the deformed meshes and contour plots of von Mises stress are given in Fig. 21 for different rotation angles.

5.5. Pinch of cylindrical shell

Pinch analysis of cylindrical shells is a nonlinear buckling benchmark for shell structures [60,61]. As discussed in Ref. [60], a cylindrical shell is considered with thickness $h = 5$, radius $R = 100$, and length $L = 200$. The Neo-Hookean model is selected with Young's modulus $E = 5$ and $\nu = 0.35$. The geometric model and two different meshes are given in Fig. 22. Due to symmetry, we consider one-half of the geometric model. The shell is meshed with 1200 hexahedral elements and 1342 polyhedral elements, respectively.

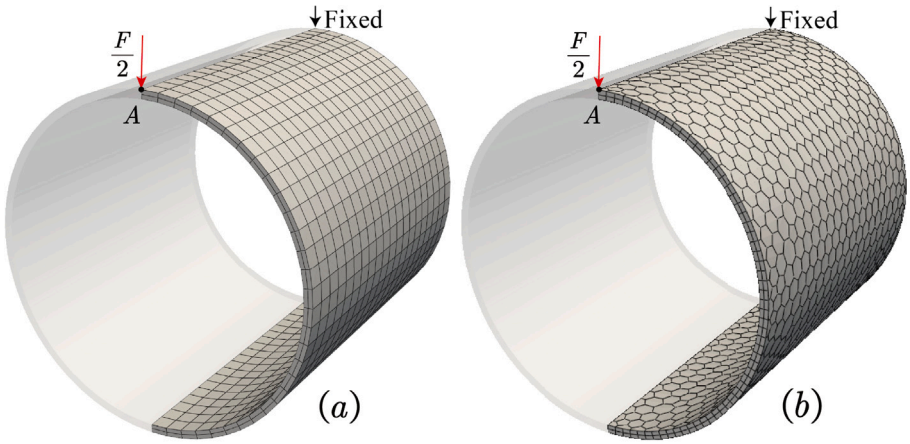

Fig. 22. Geometries and meshes for cylindrical shell, (a) hexahedral mesh, (b) polyhedral mesh.

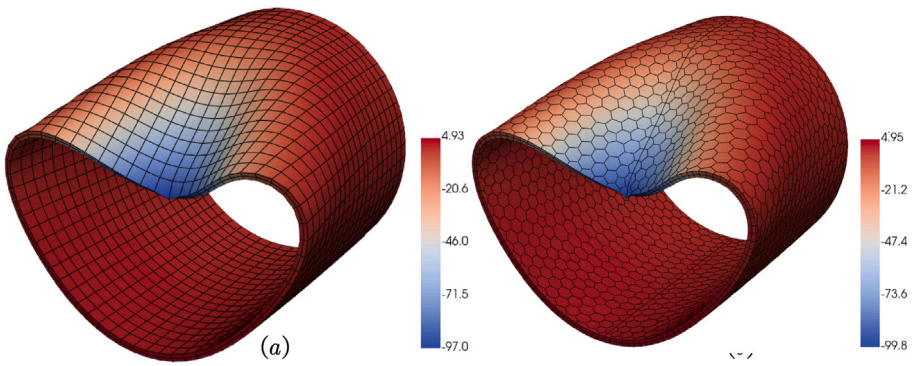

Fig. 23. Contour plots of displacement u_y and deformed shape for different meshes at last time step, (a) hexahedral mesh, (b) polyhedral mesh.

As shown in Fig. 22, one end of the cylinder is fixed, and a nodal force $F = 1$ is applied at the tip of the other end (see point A in Fig. 22). Load control and path-following techniques are necessary for computing such problems. In this work, the arc length is selected to track the response of the cylinder. The virtual element method with $k = 2$ and second-order finite element method (FEM, Q2) are selected to calculate the solutions of the cylinder. The deformed shapes of the cylinder obtained by VEM for different meshes are illustrated in Fig. 23 when the time step is 30. Besides, the deformed configuration of the cylindrical shell at various time steps for hexahedral mesh is given in Fig. 24. The load–deflection curves of the displacement u_y at point A are given in Fig. 25 for the different discretizations.

6. Conclusion

A general high-order three-dimensional virtual element method for linear and nonlinear elasticity is proposed in this work. The proposed method allows to use of general polyhedral meshes. We apply high-order VEM ($k = 2$) to three-dimensional nonlinear elastic problems for the first time. Furthermore, as a by-product, the linear elastic formulation is derived. Hence, examples include linear elastic and hyperelastic problems. Compared with the low-order VEM for elasticity, the second-order method avoids bending locking, and the results are more accurate than the first-order VEM. Since VEM can use polyhedral meshes, the hexahedral-dominated mesh can be employed for complex geometric models. Besides, locally refined meshes can be set up easily to treat fracture mechanics with VEM. It can be seen from the calculation examples that VEM is more flexible when dealing with elastic mechanics problems. In addition, due to its flexibility and accuracy, the method can be extended to other nonlinear problems. However, it should be noted that the high-order virtual element method needs to divide the polyhedral element into tetrahedral elements and then conduct numerical integration, so its calculation efficiency is lower than that of the first-order virtual element method. In order to improve calculation efficiency, point integration technology can be used in future work.

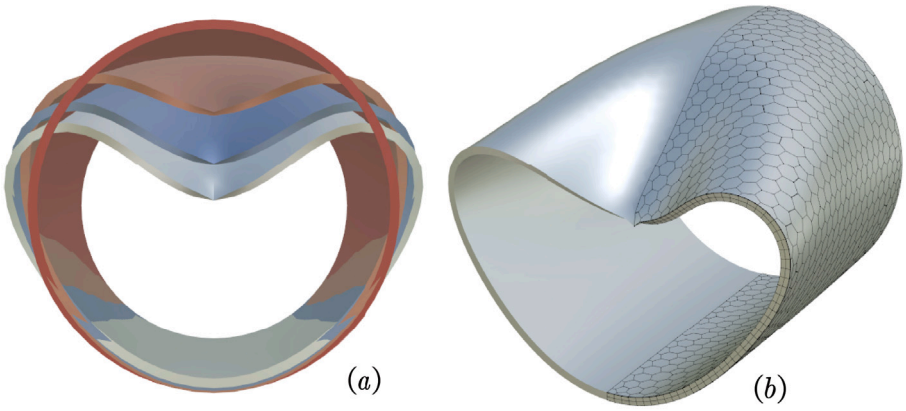

Fig. 24. Deformed configuration of the cylindrical shell for pinching problem (a) deformed configuration at various time steps for hexahedral mesh, (b) deformed configuration at the last step for polyhedral mesh.

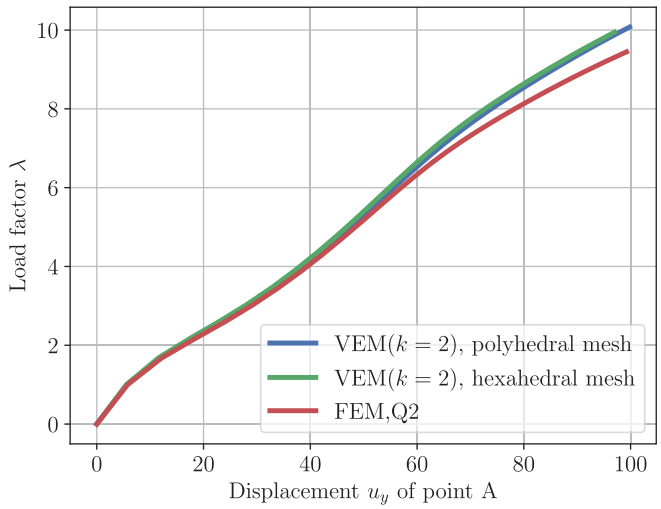

Fig. 25. Load–deflection curves of the cylindrical shell subjected to end pinching force.

CRediT authorship contribution statement

Bing-Bing Xu: Writing – review & editing, Writing – original draft, Validation, Formal analysis. **Wei-Long Fan:** Writing – original draft. **Peter Wriggers:** Writing – review & editing.

Declaration of competing interest

The authors declare the following financial interests/personal relationships which may be considered as potential competing interests: Bing-Bing Xu reports financial support was provided by Alexander von Humboldt Foundation. If there are other authors they declare that they have no known competing financial interests or personal relationships that could have appeared to influence the work reported in this paper.

Data availability

No data was used for the research described in the article.

Acknowledgment

The first and last authors are grateful for the support provided by the Alexander von Humboldt Foundation, Germany.

Appendix A. Projection operator for polygons

For a given 3D polyhedral element E whose surface $F \in \partial E$ is a planar polygon, we need to solve the local projection operator on the surface to convert the integral on the polygon surface to edges. We begin by defining the local lifting spaces on each face F

$$\tilde{\mathcal{V}}(F) := \left\{ \boldsymbol{v} \in \boldsymbol{\mathcal{H}}_1(F) : \Delta_F \boldsymbol{v} \in \boldsymbol{\mathcal{P}}_k(F), \boldsymbol{v}|_e \in \boldsymbol{\mathcal{P}}_k(e), e \in \partial F \right\}, \tag{A.1}$$

where Δ_F is the 2D Laplacian over the face F. Using the local coordinate shown in Fig. 2, the scaled monomials $\mathcal{M}_k^F$ can be defined as

$$\mathcal{M}_k^f := \left\{ m_\alpha^f = \left(\frac{\boldsymbol{\xi} - \boldsymbol{\xi}_F}{h_F} \right)^\alpha \quad \text{for} \quad \boldsymbol{\alpha} \in \mathbb{N}^{d-1} \text{ with } |\alpha| \le k \right\}. \tag{A.2}$$

For higher-order VEM, the local degrees of freedom can be selected as

- the values of $\boldsymbol{v}_p$ at the vertices of F;
- the values of the $k-1$ internal Gauss–Lobatto nodes on each edge $e \in \partial F$;
- the scaled face moments:

$$\frac{1}{|F|} \int_F \boldsymbol{v} \boldsymbol{p}_{k-2}^f \, \mathrm{d}\Omega_F, \quad \forall \boldsymbol{p}_{k-2}^f \in \boldsymbol{\mathcal{P}}_{k-2}(F). \tag{A.3}$$

Then we can define the energy projector $\Pi_{k,F}^\nabla : \tilde{\boldsymbol{\mathcal{V}}}_k(F) \to \boldsymbol{\mathcal{P}}_k(F)$:

$$\begin{cases} \displaystyle\int_F \nabla_F \Pi_{k,F}^\nabla \boldsymbol{v} \cdot \nabla_F \boldsymbol{p} \, \mathrm{d}\Omega_F = \int_F \nabla_F \boldsymbol{v} \cdot \nabla_F \boldsymbol{p} \, \mathrm{d}\Omega_F, \boldsymbol{p} \in \boldsymbol{\mathcal{P}}_k(F) \\ \displaystyle\int_F \left(\boldsymbol{v} - \Pi_{k,F}^\nabla \boldsymbol{v} \right) \mathrm{d}\Omega_F = 0 \end{cases} \tag{A.4}$$

Lastly, we get the two-dimensional virtual element space on F as

$$\mathcal{V}_k^f(F) = \left\{ \boldsymbol{v} \in \tilde{\mathcal{V}}_k^f(F) : \int_F \boldsymbol{v} \cdot \boldsymbol{q} \, \mathrm{d}\Omega_F = \int_F \left(\Pi_{k,F}^\nabla \boldsymbol{v} \right) \cdot \boldsymbol{q} \, \mathrm{d}\Omega_F, \forall \boldsymbol{q} \in \boldsymbol{\mathcal{P}}_k \backslash \boldsymbol{\mathcal{P}}_{k-2} \right\}. \tag{A.5}$$

According to the definition of degrees of freedom, we can obtain the projection operator matrix $\boldsymbol{\Pi}_{k,F}^\nabla$ according to Eq. (A.4).

Appendix B. Matrix form for hyperelastic problems

Using the Voigt notation, we have the matrix notation as

$$\boldsymbol{S} : \delta \boldsymbol{E} = \hat{\boldsymbol{S}}^T \cdot \delta \hat{\boldsymbol{E}} = \delta \hat{\boldsymbol{E}}^T \cdot \hat{\boldsymbol{S}}, \tag{B.1}$$

where $\boldsymbol{S}$ is the second Piola–Kirchhoff stress tensor and $\boldsymbol{E}$ is the Green–Lagrange strain tensor. Considering the definition of $\boldsymbol{\theta}$ in Eq. (41), we have

$$\delta \hat{\boldsymbol{E}} = \boldsymbol{A} \cdot \delta \boldsymbol{\theta} \tag{B.2}$$

where

$$\boldsymbol{A} = \begin{bmatrix} F_{11} & 0 & 0 & F_{21} & 0 & 0 & F_{31} & 0 & 0 \\ 0 & F_{12} & 0 & 0 & F_{22} & 0 & 0 & F_{32} & 0 \\ 0 & 0 & F_{13} & 0 & 0 & F_{23} & 0 & 0 & F_{33} \\ F_{12} & F_{11} & 0 & F_{22} & F_{21} & 0 & F_{32} & F_{31} & 0 \\ 0 & F_{13} & F_{12} & 0 & F_{23} & F_{22} & 0 & F_{33} & F_{32} \\ F_{13} & 0 & F_{11} & F_{23} & 0 & F_{21} & F_{33} & 0 & F_{31} \end{bmatrix}. \tag{B.3}$$

Based on the definition, we have

$$\delta \boldsymbol{E} : \boldsymbol{\mathcal{D}} : \Delta \boldsymbol{E} = \delta \hat{\boldsymbol{E}}^T \cdot \hat{\boldsymbol{D}} \cdot \Delta \hat{\boldsymbol{E}} = \delta \boldsymbol{\theta}^T \cdot \boldsymbol{A}^T \cdot \hat{\boldsymbol{D}} \cdot \boldsymbol{A} \cdot \Delta \boldsymbol{\theta} \tag{B.4}$$

$$\Delta(\delta \boldsymbol{E}) : \boldsymbol{S} = \frac{1}{2} \Delta \left(\delta \boldsymbol{F}^T \cdot \Delta \boldsymbol{F} + \Delta \boldsymbol{F}^T \cdot \delta \boldsymbol{F} \right) : \boldsymbol{S} \doteq \delta \boldsymbol{\theta}^T \cdot \boldsymbol{\mathcal{I}} \cdot \Delta \boldsymbol{\theta}, \tag{B.5}$$

where

$$\boldsymbol{\mathcal{I}} = \mathrm{diag}(\boldsymbol{S}, \boldsymbol{S}, \boldsymbol{S}) \tag{B.6}$$

Substituting Eqs. (B.4) and (B.5) into Eq. (38), Eq. (39) can be obtained lastly.

For small deformation assumption, the matrix $\tilde{\boldsymbol{A}}$ has the form as

$$\tilde{\boldsymbol{A}} = \begin{bmatrix} 1 & 0 & 0 & 0 & 0 & 0 & 0 & 0 & 0 \\ 0 & 0 & 0 & 0 & 1 & 0 & 0 & 0 & 0 \\ 0 & 0 & 0 & 0 & 0 & 0 & 0 & 0 & 1 \\ 0 & 1 & 0 & 1 & 0 & 0 & 0 & 0 & 0 \\ 0 & 0 & 0 & 0 & 0 & 1 & 0 & 1 & 0 \\ 0 & 0 & 1 & 0 & 0 & 0 & 1 & 0 & 0 \end{bmatrix}. \tag{B.7}$$

References

[1] N. Sukumar, A. Tabarraei, Conformal polygonal finite elements, Int. J. Numer. Methods Eng. 61 (2004) 2045–2066, http://dx.doi.org/10.1002/nme.1141.

[2] H. Nguyen-Xuan, A polygonal finite element method for plate analysis, Comput. Struct. 188 (2017) 45–62, http://dx.doi.org/10.1016/j.compstruc.2017.04.002.

[3] A.E. Daniele Antonio Di Pietro, Mathematical Aspects of Discontinuous Galerkin Methods, Springer, Berlin, Heidelberg, 2012.

[4] J. Hesthaven, T. Warburton, Nodal Discontinuous Galerkin Methods: Algorithms, Analysis, and Applications, vol. 54, 2007.

[5] S. Li, X. Cui, N-sided polygonal smoothed finite element method (nSFEM) with non-matching meshes and their applications for brittle fracture problems, Comput. Methods Appl. Mech. Engrg. 359 (2020) 112672, http://dx.doi.org/10.1016/j.cma.2019.112672.

[6] S.-W. Wu, G. Liu, C. Jiang, X. Liu, K. Liu, D.-T. Wan, J.-H. Yue, Arbitrary polygon mesh for elastic and elastoplastic analysis of solids using smoothed finite element method, Comput. Methods Appl. Mech. Engrg. 405 (2023) 115874, http://dx.doi.org/10.1016/j.cma.2022.115874.

[7] L. Beirao da Veiga, A. Cangiani, G. Manzini, L. Marini, A. Russo, Basic principles of virtual element methods, Math. Models Methods Appl. Sci. 23 (2012) 199–214, http://dx.doi.org/10.1142/S0218202512500492.

[8] L. Beirao da Veiga, F. Brezzi, L. Marini, A. Russo, Mixed virtual element methods for general second order elliptic problems on polygonal meshes, ESAIM Math. Model. Numer. Anal. 26 (2014) 727–747, http://dx.doi.org/10.1051/m2an/2015067.

[9] P. Wriggers, F. Aldakheel, B. Hudobivnik, Virtual Element Methods in Engineering Sciences, Springer International Publishing, 2024, http://dx.doi.org/10.1007/978-3-031-39255-9.

[10] L. Beirao da Veiga, F. Brezzi, L.D. Marini, A. Russo, The hitchhiker's guide to the virtual element method, Math. Models Methods Appl. Sci. 24 (08) (2014) 1541–1573, http://dx.doi.org/10.1142/S021820251440003X.

[11] O. Sutton, The virtual element method in 50 lines of MATLAB, Numer. Algorithms 75 (2017) http://dx.doi.org/10.1007/s11075-016-0235-3.

[12] M. Mengolini, M. Benedetto, A. Aragón, An engineering perspective to the virtual element method and its interplay with the standard finite element method, Comput. Methods Appl. Mech. Engrg. 350 (2019) 995–1023, http://dx.doi.org/10.1016/j.cma.2019.02.043.

[13] L. Beirao da Veiga, F. Brezzi, Virtual elements for linear elasticity problems, SIAM J. Numer. Anal. 51 (2) (2013) 794–812, http://dx.doi.org/10.1137/120874746.

[14] A. Gain, C. Talischi, G. Paulino, On the virtual element method for three-dimensional elasticity problems on arbitrary polyhedral meshes, Comput. Methods Appl. Mech. Engrg. 282 (2013) 132–160, http://dx.doi.org/10.1016/j.cma.2014.05.005.

[15] E. Artioli, L. Beirao da Veiga, C. Lovadina, E. Sacco, Arbitrary order 2D virtual elements for polygonal meshes: Part i, elastic problem, Comput. Mech. 60 (2017) 727–747, http://dx.doi.org/10.1007/s00466-017-1404-5.

[16] F. Dassi, C. Lovadina, M. Visinoni, A three-dimensional Hellinger–Reissner virtual element method for linear elasticity problems, Comput. Methods Appl. Mech. Engrg. 364 (2020) 112910, http://dx.doi.org/10.1016/j.cma.2020.112910.

[17] A. Ortiz-Bernardin, R. Silva-Valenzuela, S. Salinas-Fernández, N. Hitschfeld, S. Luza, B. Rebolledo, A node-based uniform strain virtual element method for compressible and nearly incompressible elasticity, Internat. J. Numer. Methods Engrg. 124 (2022) http://dx.doi.org/10.1002/nme.7189.

[18] H. Chi, G. Paulino, Some basic formulations of the virtual element method (VEM) for finite deformations, Comput. Methods Appl. Mech. Engrg. 318 (2016) 995–1023, http://dx.doi.org/10.1016/j.cma.2016.12.020.

[19] P. Wriggers, B. Reddy, W. Rust, B. Hudobivnik, Efficient virtual element formulations for compressible and incompressible finite deformations, Comput. Mech. 60 (2017) 995–1023, http://dx.doi.org/10.1007/s00466-017-1405-4.

[20] D. van Huyssteen, B. Reddy, A virtual element method for isotropic hyperelasticity, Comput. Methods Appl. Mech. Engrg. 367 (2020) 113134, http://dx.doi.org/10.1016/j.cma.2020.113134.

[21] M.L. de Bellis, P. Wriggers, B. Hudobivnik, Serendipity virtual element formulation for nonlinear elasticity, Comput. Struct. 223 (2019) 106094, http://dx.doi.org/10.1016/j.compstruc.2019.07.003.

[22] P. Wriggers, W. Rust, B. Reddy, A virtual element method for contact, Comput. Mech. 58 (2016) 995–1023, http://dx.doi.org/10.1007/s00466-016-1331-x.

[23] F. Aldakheel, B. Hudobivnik, E. Artioli, L. Beirao da Veiga, P. Wriggers, Curvilinear virtual elements for contact mechanics, Comput. Methods Appl. Mech. Engrg. 372 (2020) 113394, http://dx.doi.org/10.1016/j.cma.2020.113394.

[24] W. Shen, M. Ohsaki, J. Zhang, A 2-dimentional contact analysis using second-order virtual element method, Comput. Mech. 70 (2022) 995–1023, http://dx.doi.org/10.1007/s00466-022-02165-y.

[25] M. Cihan, B. Hudobivnik, J. Korelc, P. Wriggers, A virtual element method for 3D contact problems with non-conforming meshes, Comput. Methods Appl. Mech. Engrg. 402 (2022) 115385, http://dx.doi.org/10.1016/j.cma.2022.115385.

[26] P. Wriggers, B. Hudobivnik, A low order virtual element formulation for finite elasto-plastic deformations, Comput. Methods Appl. Mech. Engrg. 327 (2017) 4702–4725, http://dx.doi.org/10.1016/j.cma.2017.08.053.

[27] B. Hudobivnik, F. Aldakheel, P. Wriggers, A low order 3D virtual element formulation for finite elasto–plastic deformations, Comput. Mech. 63 (2019) 4702–4725, http://dx.doi.org/10.1007/s00466-018-1593-6.

[28] M. Cihan, B. Hudobivnik, F. Aldakheel, P. Wriggers, 3D mixed virtual element formulation for dynamic elasto-plastic analysis, Comput. Mech. 68 (2021) 1–18, http://dx.doi.org/10.1007/s00466-021-02010-8.

[29] A.L. Gain, G.H. Paulino, L.S. Duarte, I.F. Menezes, Topology optimization using polytopes, Comput. Methods Appl. Mech. Engrg. 293 (2015) 411–430, http://dx.doi.org/10.1016/j.cma.2015.05.007.

[30] S. Ding, Y. Huang, X. Cui, Y. Fan, An improved integrated framework based nodal density variable and voronoi polygon for FE-based topology optimization, Comput. Struct. 292 (2024) 107244, http://dx.doi.org/10.1016/j.compstruc.2023.107244.

[31] K. Park, H. Chi, G. Paulino, On nonconvex meshes for elastodynamics using virtual element methods with explicit time integration, Comput. Methods Appl. Mech. Engrg. 356 (2019) 669–684, http://dx.doi.org/10.1016/j.cma.2019.06.031.

[32] K. Park, H. Chi, G. Paulino, Numerical recipes for elastodynamic virtual element methods with explicit time integration, Internat. J. Numer. Methods Engrg. 121 (2019) 1–31, http://dx.doi.org/10.1002/nme.6173.

[33] M. Cihan, B. Hudobivnik, F. Aldakheel, P. Wriggers, Virtual element formulation for finite strain elastodynamics, Comput. Model. Eng. Sci. 129 (2021) 1151–1180, http://dx.doi.org/10.32604/cmes.2021.016851.

[34] N. Sukumar, M. Tupek, Virtual elements on agglomerated finite elements to increase the critical time step in elastodynamic simulations, Internat. J. Numer. Methods Engrg. 123 (2022) 4702–4725, http://dx.doi.org/10.1002/nme.7052.
[35] T.-R. Liu, F. Aldakheel, M. Aliabadi, Virtual element method for phase field modeling of dynamic fracture, Comput. Methods Appl. Mech. Engrg. 411 (2023) 116050, http://dx.doi.org/10.1016/j.cma.2023.116050.
[36] F. Aldakheel, B. Hudobivnik, P. Wriggers, Virtual element formulation for phase-field modeling of ductile fracture, Int. J. Multiscale Comput. Eng. 17 (2019) 181–200, http://dx.doi.org/10.1615/IntJMultCompEng.2018026804.
[37] Z. Zheng, U. Nackenhorst, Stochastic virtual element methods for uncertainty propagation of stochastic linear elasticity, Comput. Mech. (2023) http://dx.doi.org/10.1007/s00466-023-02384-x.
[38] L. Beirao da Veiga, A. Chernov, L. Mascotto, A. Russo, Basic principles of hp virtual elements on quasiuniform meshes, Math. Models Methods Appl. Sci. 26 (2015) http://dx.doi.org/10.1142/S021820251650038X.
[39] L. Mascotto, L. Beirao da Veiga, A. Chernov, A. Russo, Exponential convergence of the hp virtual element method with corner singularities, Numer. Math. 138 (2018) http://dx.doi.org/10.1007/s00211-017-0921-7.
[40] P. Wriggers, B. Hudobivnik, F. Aldakheel, NURBS-based geometries: A mapping approach for virtual serendipity elements, Comput. Methods Appl. Mech. Engrg. 378 (2021) 113732, http://dx.doi.org/10.1016/j.cma.2021.113732.
[41] M. Nale, C. Gatta, D. Addessi, E. Benvenuti, E. Sacco, An enhanced corotational virtual element method for large displacements in plane elasticity, Comput. Mech. (2024) 1–14, http://dx.doi.org/10.1007/s00466-023-02437-1.
[42] E. Artioli, L. Veiva, C. Lovadina, E. Sacco, Arbitrary order 2D virtual elements for polygonal meshes: Part II, inelastic problem, Comput. Mech. 60 (2017) http://dx.doi.org/10.1007/s00466-017-1429-9.
[43] P. Wriggers, M. De Bellis, B. Hudobivnik, A taylor-hood type virtual element formulations for large incompressible strains, Comput. Methods Appl. Mech. Engrg. 385 (2021) 114021, http://dx.doi.org/10.1016/j.cma.2021.114021.
[44] H. Chi, L. Beirao da Veiga, G.H. Paulino, A simple and effective gradient recovery scheme and a posteriori error estimator for the virtual element method (VEM), Comput. Methods Appl. Mech. Engrg. 347 (2019) 21–58, http://dx.doi.org/10.1016/j.cma.2018.08.014.
[45] L. Beirao da Veiga, F. Dassi, A. Russo, High-order virtual element method on polyhedral meshes, Comput. Math. Appl. 74 (5) (2017) 1110–1122, http://dx.doi.org/10.1016/j.camwa.2017.03.021.
[46] F. Dassi, L. Mascotto, Exploring high-order three dimensional virtual elements: Bases and stabilizations, Comput. Math. Appl. 75 (9) (2018) 3379–3401, http://dx.doi.org/10.1016/j.camwa.2018.02.005.
[47] J. Huang, Y. Yu, Some estimates for virtual element methods in three dimensions, Comput. Methods Appl. Math. 23 (2022) http://dx.doi.org/10.1515/cmam-2022-0062.
[48] M. Visinoni, A family of three-dimensional virtual elements for Hellinger–Reissner elasticity problems, Comput. Math. Appl. 155 (2024) 97–109, http://dx.doi.org/10.1016/j.camwa.2023.11.034.
[49] S. Berrone, A. Borio, F. Marcon, G. Teora, A first-order stabilization-free virtual element method, Appl. Math. Lett. 142 (2023) 108641, http://dx.doi.org/10.1016/j.aml.2023.108641.
[50] A. Lamperti, M. Cremonesi, U. Perego, A. Russo, C. Lovadina, A hu-washizu variational approach to self-stabilized virtual elements: 2D linear elastostatics, Comput. Mech. 71 (2023) 1–21, http://dx.doi.org/10.1007/s00466-023-02282-2.
[51] S. Berrone, A. Borio, F. Marcon, Lowest order stabilization free virtual element method for the Poisson equation, 2021, arXiv preprint 2103.16896.
[52] S. Berrone, A. Borio, F. Marcon, A stabilization-free virtual element method based on divergence-free projections, Comput. Methods Appl. Mech. Engrg. 424 (2024) 116885, http://dx.doi.org/10.1016/j.cma.2024.116885.
[53] B.-B. Xu, P. Wriggers, 3D stabilization-free virtual element method for linear elastic analysis, Comput. Methods Appl. Mech. Engrg. 421 (2024) 116826, http://dx.doi.org/10.1016/j.cma.2024.116826.
[54] A. Chen, N. Sukumar, Stabilization-free virtual element method for plane elasticity, Comput. Math. Appl. 138 (2023) 88–105, http://dx.doi.org/10.1016/j.camwa.2023.03.002.
[55] B.-B. Xu, F. Peng, P. Wriggers, Stabilization-free virtual element method for finite strain applications, Comput. Methods Appl. Mech. Engrg. 417 (2023) 116555, http://dx.doi.org/10.1016/j.cma.2023.116555.
[56] T. Sorgente, S. Biasotti, G. Manzini, M. Spagnuolo, Polyhedral mesh quality indicator for the virtual element method, Comput. Math. Appl. 114 (2022) 151–160, http://dx.doi.org/10.1016/j.camwa.2022.03.042.
[57] P. Wriggers, Nonlinear Finite Element Methods, Springer Verlag, 2008, http://dx.doi.org/10.1007/978-3-642-56865-7.
[58] J. Korelc, P. Wriggers, Automation of Finite Element Methods, Springer International Publishing, 2016, URL https://books.google.de/books?id=gg1kDAAAQBAJ.
[59] L. Beirao da Veiga, C. Lovadina, D. Mora, A virtual element method for elastic and inelastic problems on polytope meshes, Comput. Methods Appl. Mech. Engrg. 295 (2015) 327–346, http://dx.doi.org/10.1016/j.cma.2015.07.013, URL https://www.sciencedirect.com/science/article/pii/S004578251500225X.
[60] R. Poya, R. Ortigosa, A. Gil, Variational schemes and mixed finite elements for large strain isotropic elasticity in principal stretches: Closed-form tangent eigensystems, convexity conditions, and stabilised elasticity, Internat. J. Numer. Methods Engrg. 124 (2023) http://dx.doi.org/10.1002/nme.7254.
[61] K. Sze, X. Liu, S. Lo, Popular benchmark problems for geometric nonlinear analysis of shells, Finite Elem. Anal. Des. 40 (11) (2004) 1551–1569, http://dx.doi.org/10.1016/j.finel.2003.11.001.